Ocean Engineering 364 (2026) 126963

Contents lists available at ScienceDirect

Ocean Engineering

journal homepage: www.elsevier.com/locate/oceaneng

Research paper

Hydrodynamic investigation of a novel wave-powered unmanned surface vehicle

Milad Zabihi [a,*], V.V.S. Sricharan [a], Ayse Nur Karayel [a], Brendan McGrath [b], Patrick Duffy [b], Jimmy Murphy [a]

[a] MaREI Centre, University College Cork, Cork, Ireland
[b] Jospa Ocean Solutions Ltd., Dublin, Ireland

ARTICLE INFO

Keywords:
Wave tank experiments
Wave energy
Renewable energy
Hydrodynamic
Orbital velocity
Unmanned surface vehicle

ABSTRACT

Traditional Unmanned Surface Vehicles (USVs) have typically relied on batteries or fossil fuels for propulsion, presenting challenges related to limited endurance, operational range, and carbon emissions. This paper introduces a pioneering USV design that harnesses only the orbital motion of the wave particles as its primary propulsion source. The USV consisting of multiple fin modules can move along and against the wave propagation direction. A 1:20 scale model was fabricated by Jospa Ltd and tested at the Lir National Ocean Test Facility at University College Cork. The effects of hydrodynamic and geometrical factors on the device performance including its pulling capacity and velocity were studied. The USV performs best with 45° forward fins for wave-following motion and 45° backward fins for wave-opposing motion. Increasing wave height improves the model performance with results showing that doubling the wave height increases its velocity by 65% to 140%. Additionally, reducing fin spacing could significantly improve the model's performance. A numerical model based on potential wave theory was also developed and validated using experiments. The numerical sensitivity analysis showed that the 45° fin configuration provided the strongest and most consistent overall propulsion performance across the investigated wave periods and operating directions.

1. Introduction

The ocean is of immense importance to our planet, playing a critical role in sustaining life and shaping Earth's climate. It covers about 70% of the Earth's surface and provides habitats for a lot of marine species. Beyond its ecological significance, the ocean is also a crucial source of food, energy, and resources for human societies. Recently, Unmanned Surface Vehicles (USVs) have emerged as extremely useful tool in ocean operations, propelling ocean exploration into a new era (Er et al., 2023; Liu et al., 2016; Petersen et al., 2016).

USVs are autonomous vehicles designed to carry out tasks in diverse and complex environments, operating without human intervention (Breivik, 2010). Apart from ocean exploration, USVs can be used for transportation such as towing offshore structures or even collecting plastics from the ocean surface. Different types of USV applications are summarized by (Liu et al., 2016). Amongst their applications, bathymetric surveys (Rasal, 2013; Roberts and Sutton, 2006), environmental sampling and monitoring (Caccia et al., 2005; Švec et al., 2014), pollution measurement and cleanup, oil and gas exploration (Pastore and Djapic, 2010), offshore structures construction, maintenance (Breivik et al., 2008) and transportation (Kiencke et al., 2006) are the most prominent. A comparison of USVs with other manned systems was conducted by (Liu et al., 2016) where they concluded some advantages of USVs over manned vehicles. The two main advantages of USVs over manned vessels are their ability to undertake high-risk missions without endangering personnel and their greater potential payload capacity for operations in deeper waters (Liu et al., 2016). To gain insight into the developed prototype vessels and fundamental design considerations, readers may also refer to (Bertram, 2008; Manley, 2008; Motwani, 2012).

Currently, the majority of commercially available USVs and Unmanned Underwater Vehicles (UUVs) rely on batteries such as alkaline batteries and fuel cells as their power source (Boscaino et al., 2021; Wang et al., 2012). However, batteries have some limitations due to their limited energy capacity. These drawbacks include restricted travel distance, insufficient capability for frequent sampling, and the risk of

* Corresponding author. MaREI Centre, University College Cork, Cork, Ireland
E-mail address: m.zabihi@ucc.ie (M. Zabihi).

https://doi.org/10.1016/j.oceaneng.2026.126963
Received 13 May 2026; Received in revised form 7 July 2026; Accepted 7 July 2026
Available online 10 July 2026

marine pollution when they are damaged. They also require regular recharging and relocation from a specialized host platform or support vessel, a process that can be both costly and inconvenient (Yang and Martinez, 2023).

In comparison to batteries, renewable energy sources can provide a consistent and considerably cleaner energy supply to USVs, thereby significantly reducing the potential for polluting the ocean environment when utilized. As a result, renewable energy is widely acknowledged as the primary energy supply for the next generation of USVs. Reviewing the literature shows that solar energy and ocean temperature gradients have been already used to power unmanned underwater vehicle called SAUV-II and SOLO-TREC (Chao, 2016; Crimmins et al., 2006). However, SAUV-II must spend all the daylight time for recharging and only the nighttime for missions (Yang and Martinez, 2023). An Autonomous Surface Vehicle (ASV) powered by solar energy was also developed by (Sornek et al., 2022) to monitor water quality. Several alternative technologies have also showcased the utilization of renewable energy sources to directly power surface propulsion instead of relying on battery recharging. An exemplary UUV known as the "Ocean Aero Submaran" effectively utilizes wind energy.

There are also various types of ocean renewable energies such as tidal, wave, temperature, and salinity gradients (Rehman et al., 2023) that can be used as power supplies for USVs. Among them, wave energy offers several advantages over other forms of ocean renewable energies. Waves tend to be more consistent (Donelan et al., 1997) and predictable than some other renewable sources like wind or solar energy. This consistency can be advantageous for continuous propulsion of USVs without relying on intermittent energy sources. Waves have a higher energy density compared to wind or solar energy (Samad and Suchithra, 2021; Veerabhadrappa et al., 2022). This means that a smaller and more compact system can generate a significant amount of energy, making it well-suited for space-limited applications like autonomous surface and underwater vehicles. This high energy density not only enhances efficiency but also minimizes the environmental footprint by utilizing less space compared to large-scale wind or solar installations. These features make ocean waves an excellent choice for supplying energy to USVs to enable them to recharge autonomously.

UUVs which utilise wave energy includes Wave Glider SV2 and SV3 developed by Liquid Robotics which make use of wave energy (Hine et al., 2009; Manley and Willcox, 2010; Willcox et al., 2009). The Wave Glider consists of two primary components: a surface float and a submerged glider, interconnected by a tether (Manley and Willcox, 2010). By converting ocean wave energy into forward thrust, the glider can move forward. Other autonomous underwater vehicles powered by wave energy can be found in (Ding et al., 2015; Townsend, 2016; Townsend and Shenoi, 2016; Zhang et al., 2021). Even though researchers developed numerous wave energy devices (Falcao, 2010; López et al., 2013), the transfer of wave power to the USV or any other kind of either autonomous underwater or surface vehicle has been a challenge. Among different types of wave energy devices developed, technologies like spar buoy which make use of an enclosed mass-spring-damper system for power take off (PTO) system can be considered to transfer power to the USVs as they are portable and compact. However, tuning the resonant frequency of the WEC device with the waves to get the highest efficiency is challenging and requires a massive and bulky WEC (Yang and Martinez, 2023).

The main purpose of the current research is to introduce a new concept developed by Jospa Ocean Solutions. The developed device is called Orbital Robotics – Clean Automation (OR-CA) which utilizes wave energy instead of fossil fuels for towing devices such as data gathering sensors, i.e., acoustic array. It can also be used as a USV in scientific applications. The proposed technology uses the orbital motion of the wave particles to move forward or backward or to turn while there is no PTO system installed on the device. The device can provide significant advantages over conventionally powered, crewed vessels, that have cost, health and safety, and other practical considerations particularly during the performance of long voyages. The concept is also totally environmentally friendly in terms of carbon emission and noise pollution. This study is the first research; to the best of the authors knowledge, that investigates a wave powered USV utilizing wave orbital motion to tow a device in different wave conditions. The paper investigates the effect of different hydrodynamic and geometric factors on the device performance including its velocity and pulling force both numerically and experimentally. The paper is organized as follows. In Section 2, the model working principle is explained. In Section 3, experimental setup including all the instrumentation used as well as the model characteristics are explained in detail. Section 4 introduces the development of the numerical model using OrcaFlex. Section 5 presents experimental results and discusses the effects of geometrical and hydrodynamic parameters on the model performance. It also includes concept validation using numerical results. Finally, Section 6 summarizes the main findings of this experimental campaign backed by numerical analysis.

2. Working principle and theoretical framework

2.1. Device description and propulsion mechanism

The wave-propelled USV investigated in this study harvests energy from ocean surface waves to generate thrust without any on-board propulsion machinery. The OR-CA device can be understood as a modular wave-driven propulsion system composed of rear propulsion modules and one front steering module. Each module consists of four main structural sub-systems: the surface float/body, the submerged fin assemblies, the passive hinge-stopper mechanism and the actuators which are controlled by a radio controller. The surface body provides buoyancy and follows the incident wave-induced motions. The fins are mounted on passive hinges, allowing rotation relative to the supporting frame. However, their rotation is limited in one direction by a mechanical stopper. The actuators shown in Fig. 1 are configuration control actuators rather than propulsion actuators. They are used to set or adjust the fin-stopper configuration for forward/backward operation and to control the steering-module fin angle. In the present experiments, these settings were prescribed before each test, and the actuators remained inactive during the wave runs. Therefore, the fins rotated passively under wave-induced hydrodynamic loading, with their angular motion limited by the mechanical stoppers. In practical operation, the same actuators are activated only when a change in propulsion direction or steering is required, either autonomously by the onboard guidance and control system or manually via remote operator commands. Once the desired configuration is established, the actuators are switched off, and the vehicle continues to propel itself passively using wave energy until the next reconfiguration command.

The principal structural components comprise PETG fins supported by a carbon-fibre tubular spine. The PETG has a typical Young's modulus of approximately 1.9–2.3 GPa, while the carbon-fibre spine has a Young's modulus of approximately 170 GPa. The structural members within each individual module were represented as rigid bodies under the investigated loading conditions. However, adjacent modules were connected through compliant joints that permitted limited relative rotation, so the complete multi-module assembly was not treated as a single rigid structure. The fins rotated independently about their hinge axes until their motion was restricted by the mechanical stoppers. Structural deformation including twisting of the fins and supporting spine was outside the scope of the present study. The different structural parts of a representative rear and steering module are shown in Fig. 1.

The rear modules primarily generate longitudinal thrust, while the steering module introduces an azimuth angle to the front fins so that part of the hydrodynamic force has a transverse component. This transverse component can generate a yaw moment and therefore provide directional control. Fig. 2 gives an overall schematic of the design with steering module at the front followed by four rear modules. The azimuth

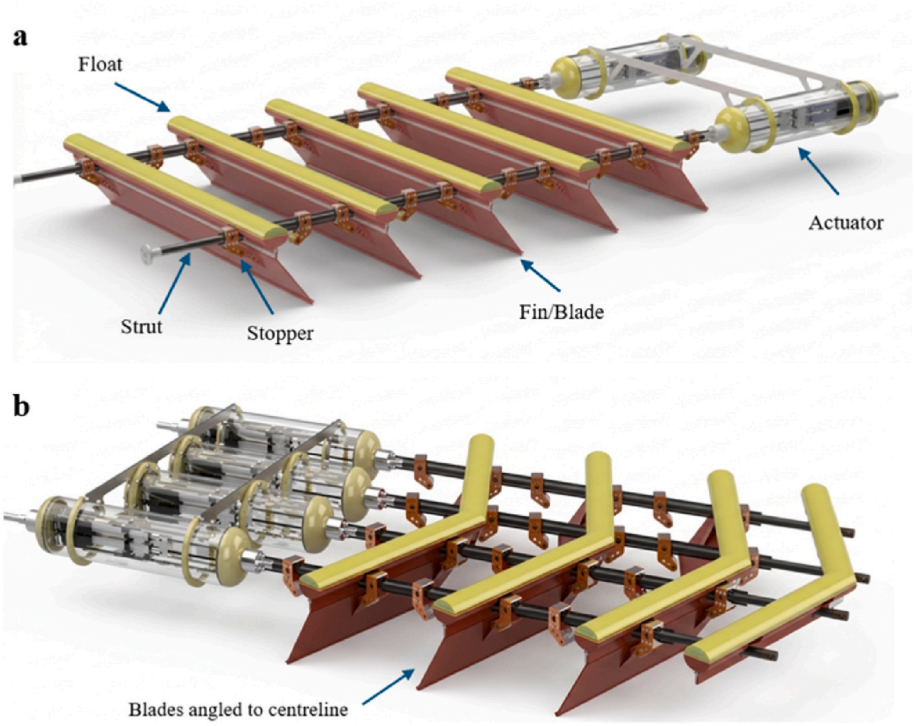

Fig. 1. a) rear module, b) steering module. The actuators are used for configuration control and do not actively drive the fins during wave-induced propulsion.

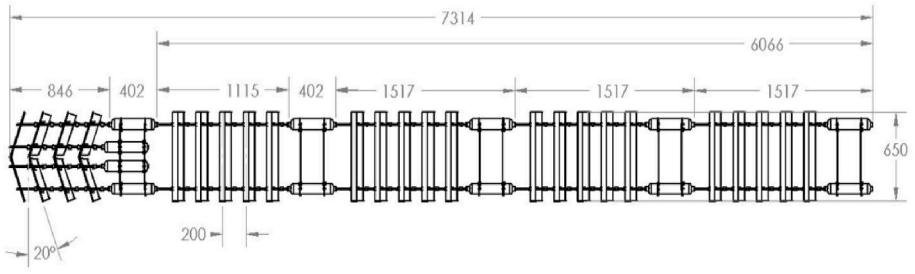

Fig. 2. Schematic overview of the model dimensions in mm.

angle of the fins in all rear modules is 0° whereas that of the steering module fins is 20°.

The prominent feature of the present design is the ability to select the direction of propulsion, either forward (in the direction of wave propagation) or backward (against the direction of wave propagation) through the physical orientation of the fin assemblies alone, without any active control input. At each fin-float interface, there is a stopper mechanism, which is pre-set. Beyond this pre-set angle, the stopper restricts the fin's rotation. As illustrated in Fig. 3, in the forward mode the fins are inclined at 45° such that their lower edge points in the direction of wave advance (orientation "\"), whilst in the backward mode the orientation ("/") is reversed, with the lower edge pointing against the wave direction. The solid red lines represent the stopper-limited positions at 45°, while the dashed lines indicate the fins rotational range from 0°; aligned with the hull, to 45°.

During one wave half-cycle, the fin reaches the stopper and resists the incoming flow, thereby generating thrust. During the opposite half-cycle, it rotates freely and feathers, producing comparatively little force.

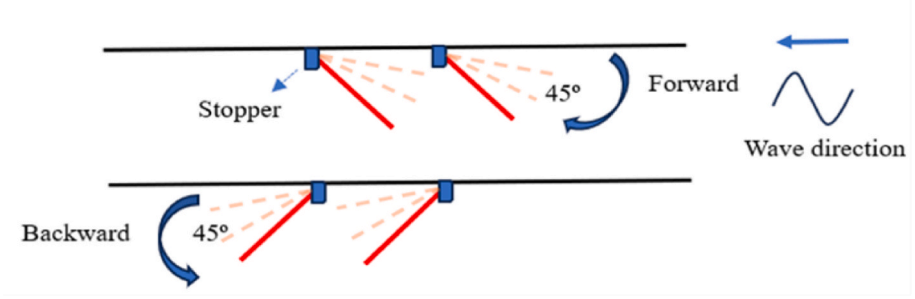

Fig. 3. Definition of the angle of the fin including extreme positions and wave direction.

This asymmetric response prevents the forces from cancelling over a complete wave cycle. The operation of the two propulsion modes is summarized in Table 1, with reference to Fig. 3.

Reversing the fin orientation therefore changes the active half-cycle and reverses the propulsion direction. The resulting performance also depends on the wave period, fin arrangement and inter-module spacing.

2.2. Wave kinematics

The free-surface elevation based on linear wave theory is described as:

$$\eta(x,t) = \frac{H}{2}\cos(kx - \omega t) \tag{1}$$

where H is the wave height, $k = 2\pi/L$ is the wavenumber, L is the wavelength, $\omega = 2\pi/T$ is the angular frequency, and T is the wave period. The linear dispersion relation relates these quantities through the water depth, d:

$$\omega^2 = gk\tanh kd \tag{2}$$

Throughout this work, the x-axis is defined in the direction of wave propagation, the z-axis is positive upward from the mean water level, and the wave travels in the positive x-direction during the forward mode and in the negative x-direction in the backward mode.

The orbital velocity and acceleration components of the fluid particles at depth z are

$$u_x(z,t) = \frac{H}{2}\,\omega\,\frac{\cosh k(d+z)}{\sinh kd}\cos\theta \tag{3}$$

$$a_x(z,t) = \frac{H}{2}\omega^2\frac{\cosh k(d+z)}{\sinh kd}\sin\theta \tag{4}$$

$$u_z(z,t) = \frac{H}{2}\,\omega\,\frac{\sinh k(d+z)}{\sinh kd}\sin\theta \tag{5}$$

$$a_z(z,t) = -\frac{H}{2}\omega^2\frac{\sinh k(d+z)}{\sinh kd}\cos\theta \tag{6}$$

where, u_x and a_x are horizontal velocity and acceleration of a water particle, while u_z and a_z are vertical velocity and acceleration of a water particle. z is the distance from the still water level, and $\theta = kx - \omega t$ is the phase angle where t is time and x is the horizontal coordinate. The horizontal and vertical orbital velocity components are 90° out of phase in time. This phase relationship is fundamental to the thrust-generation mechanism: at the wave crest, the horizontal orbital velocity is at its maximum whilst the vertical component is zero, and vice versa at the quarter-wave positions.

Table 2 shows the theoretical maximum orbital velocities and accelerations for different wave conditions tested in this study. The orbital velocities and accelerations decrease while wave period increases.

The linear wave kinematics are used only to define the dominant orbital velocities acting at the fin depth. Second-order effects such as Stokes drift were not explicitly included in the numerical model; therefore, the propulsion mechanism is attributed primarily to nonlinear drag rectification caused by the passive hinge-stopper mechanism.

Table 1
Half-cycle force rectification in forward and backward propulsion modes.

Mode	Wave half-cycle	Fin state	Net Thrust
Forward (\)	Upstroke (crest)	Locked at 45°, active	« Thrust (with waves)
Forward (\)	Downstroke (trough)	Free to feather, passive	≈ 0
Backward (/)	Downstroke (trough)	Locked at 45°, active	» Thrust (against waves)
Backward (/)	Upstroke (crest)	Free to feather, passive	≈ 0

Table 2
Horizontal and vertical components of orbital velocities and accelerations for the tested regular wave conditions.

$H\,[m]$	$T\,[s]$	$u_x\,[m/s]$	$a_x\,[m/s^2]$	$u_z\,[m/s]$	$a_z\,[m/s^2]$
0.2	1.342	0.467	2.19	0.467	2.19
0.2	1.789	0.351	1.23	0.351	1.23
0.2	2.236	0.286	0.80	0.282	0.79
0.2	2.683	0.248	0.58	0.235	0.55
0.2	3.130	0.228	0.46	0.201	0.40
0.4	1.342	0.937	4.39	0.937	4.39
0.4	1.789	0.702	2.47	0.702	2.47
0.4	2.236	0.570	1.60	0.561	1.58
0.4	2.683	0.496	1.16	0.467	1.10
0.4	3.130	0.454	0.91	0.402	0.81

2.3. Equation of motion

The response of the USV to the wave loads can be represented with the following equation of motion in six degrees of freedom.

$$M\,\ddot{\xi}(t) = F_{\xi}^{FK}(t) + F_{\xi}^{D}(t) + F_{\xi}^{R}(t) + F_{\xi}^{blade}(t) \tag{7}$$

where M is the 6×6 structural mass matrix, and ξ is a 6×1 displacement vector. $\ddot{\xi}$ is the acceleration vector and F^{FK}, F^{D}, F^{R}, and F^{blade} represent Froude-Krylov (F-K), diffraction, and radiation, together with the viscous force arising from the submerged fin assemblies, respectively.

The diffraction parameter $\frac{D}{L} < 0.2$ confirms that the scattering effect can be considered negligible. Any net propulsion must arise from nonlinear hydrodynamic mechanisms, predominantly inertia and viscous drag acting on geometrically asymmetric elements undergoing oscillatory motion. Therefore, the hydrodynamic forces acting on the USV can be represented using the Morison equation.

$$F_{translational} = \rho\,C_{m,i}\,V_b\dot{u}_f + \frac{1}{2}\rho C_{D,i}\,A_i\,|V_{rel}|V_{rel} \tag{8}$$

where C_m is the inertia coefficient, accounts for the added mass of fluid that accelerates with the body, V_b is the displaced volume, $\dot{u}_f$ is the undisturbed local fluid acceleration at the fin location, C_D is the drag coefficient, A_i is the projected area of the fin, and V_{rel} is the relative velocity between the undisturbed local fluid and the fin body.

For a slender body like a fin with planform area A subjected to a relative flow of magnitude $|V_{rel}|$, the normal drag force can be expressed as

$$N(t) = \frac{1}{2}\,\rho\,C_N^*\,A\,|V_{rel}|^2 \tag{9}$$

where ρ is the water density and C_N^* is the effective normal force coefficient. A critical distinction must be made between C_N^* and the classical quasi-steady normal force coefficient (C_D) which is typically of the order of 1.5-2.0 for a thin plate in steady flow. In the present configuration, however, C_N^* serves as an effective lumped hydrodynamic force coefficient that implicitly encapsulates several coupled physical mechanisms that quasi-steady theory does not solve. The C_N^* acts as a rectification factor, lumping unsteady separation, angle-of-attack effects, mass transport in the form of Stokes drift, 3D flow effects and partial shielding.

Although these mechanisms may be physically present in the experiments, explicitly capturing each of these is outside the scope of this study. It is to be noted that C_N^* was not measured in the experimental programme. Its determination is achieved through systematic calibration of the numerical model against measured USV surge velocity. The calibrated values should be interpreted as system-level effective parameters, valid within the range of wave conditions tested, rather than

as intrinsic geometric properties of the fin alone.

At any instant, the fin assembly undergoes both surge (horizontal) and heave (vertical) motion as the float responds to the incident wave. The fluid velocity experienced by the fin in its local frame, referred to as the relative velocity, is therefore the vector difference between the undisturbed orbital fluid velocity and the fin body velocity.

$$V_{rel} = (u_x - \dot{X})\,\hat{x} + (u_z - \dot{z}_{float})\,\hat{z} \tag{10}$$

where $\dot{X}$ is the instantaneous surge velocity of the USV and $\dot{z}_{float}$ is the heave velocity of the float-fin assembly. The magnitude of the relative velocity is

$$|V_{rel}| = \sqrt{(u_x - \dot{X})^2 + (u_z - \dot{z}_{float})^2} \tag{11}$$

The instantaneous angle of attack experienced by the fin that is the angle between the relative velocity vector and the fin chord line is,

$$\alpha(t) = \beta - \tan^{-1}\left[\frac{u_x - \dot{X}}{u_z - \dot{z}_{float}}\right] \tag{12}$$

where β is the inclination angle of the fin. The angle of attack therefore varies continuously over the wave cycle as both the fluid orbital velocities and the float motion evolve. The surge and heave force components (T_x, T_z) acting on a fin are:

$$T_x(t) = N(t)\,sin\,\beta = \frac{1}{2}\,\rho\,C_N^*\,A\,|V_{rel}|^2\,\sin\beta \tag{13a}$$

$$T_z(t) = N(t)\,cos\,\beta = \frac{1}{2}\,\rho\,C_N^*\,A\,|V_{rel}|^2\,\cos\beta \tag{13b}$$

The rotational dynamics of the fin are governed by

$$I_{fin}\ddot{\theta} = M_{hydro}(\theta, \dot{\theta}, V_{rel}) - M_{stopper}(\theta) \tag{14}$$

M_{hydro} represents the hydrodynamic moment acting on the fin due to fluid forces generated by the relative flow velocity. I_{fin} is the fin moment of inertia and $M_{stopper}$ is the constraint moment applied by the mechanical stopper. The stopper enforces the directional rectification mechanism by restricting rotation during the active half-cycle while allowing free motion during the passive half-cycle.

3. Experimental setup and model description

The experiments were conducted at Lir National Ocean Test Facility (Lir NOTF), MaREI Centre, University College Cork, Ireland. There are four tanks at Lir NOTF of various scales and depths for emulation of ocean waves and currents. The tests were conducted in the Deep Ocean Basin (DOB) which is 35 m long, 12 m wide and has a maximum depth of 3 m (Fig. 4). The basin is equipped with a moveable floor to vary the water depth. The floor can be raised above water level to safely install models and their moorings.

The 1:20 scale OR-CA model was composed of a flexible frame on which different modules were mounted. In addition to one steering module, there were five other modules which were all connected. The performance of the device was tested with four and five modules while it was connected to the steering module. It is noted that each module includes five fins except the steering module, which has four inclined fins (20°) (Fig. 5). The rotation of these fins is limited by a series of stoppers, the position of which is linked to radio-controlled servomotors located in the control boxes. The other modules are shown in Fig. 6.

Each module weight is 5.67 kg, and the steering module weight is 8.22 kg, including control boxes. The radio-guided stoppers allowed the operator to limit and set the fin angle to a certain value before each test. An example of a 45-degree fin angle used in this study is shown in Fig. 3. A “Forward” angle is an angle that directs the fin's movement towards its fore, which leads the device to move along the wave propagation direction, and “Backward” angles do the opposite.

Regardless of the number of modules, two types of setups were considered. The first setup, which is shown on the left hand side of Fig. 7, was a stationary setup used to measure the average force applied by the device (towing force). The red arrow shows the position of the mooring line tied to the vertical stationary column. A load cell connected to this mooring line was used to measure the force. The mooring line was taut and tied horizontally at rest so as to keep the load cell as parallel as possible to the wave propagation direction. In addition to stationary testing, some tests were designed to calculate the towing speed. The 35 m length of the tank allowed for testing the velocity of the device in different wave conditions. The nonstationary setup is shown in right hand side of Fig. 7.

For this test campaign, two 45.36 kg Futek load cells (Model LSB 210) were placed in the mooring lines to measure the mooring line tension. These load cells were calibrated beforehand, and the maximum errors recorded during calibration are presented in Table 3. Seven wave gauges were placed in the deep ocean basin. All were used upstream of the model along the wave propagation axis. They were used to monitor the wave height and period during the tests. Calibration errors found during the calibration of the wave gauges are shown in Table 4. Qualisys software was used to track the movement of the model with multiple markers placed at both ends of the model. The aim was to measure the velocity of the device along and against the wave propagation direction. The average residual error of the cameras after calibration was 0.75 mm.

The test plan consisted of 10 regular waves. The wave conditions which were used are described in Table 5, and the list of different fin angles is presented in Table 6. Since the wave-induced motion of the floating body is primarily governed by gravity, Froude similarity was adopted for scaling between model and full scale. The length scale ratio is therefore ($\lambda = \frac{L_p}{L_m}$) where the subscripts (p) and (m) denote prototype and model scale, respectively. According to Froude scaling, time and

Fig. 4. Deep ocean basin at lir national ocean test facility.

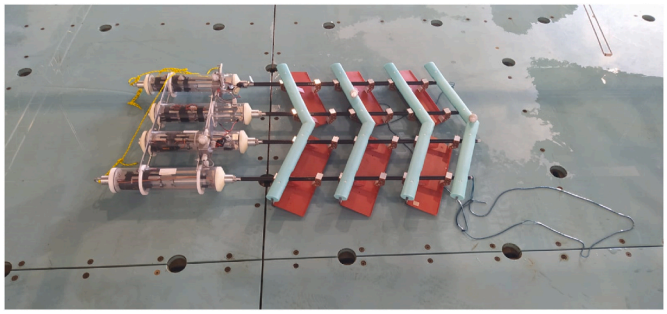

Fig. 5. Steering module.

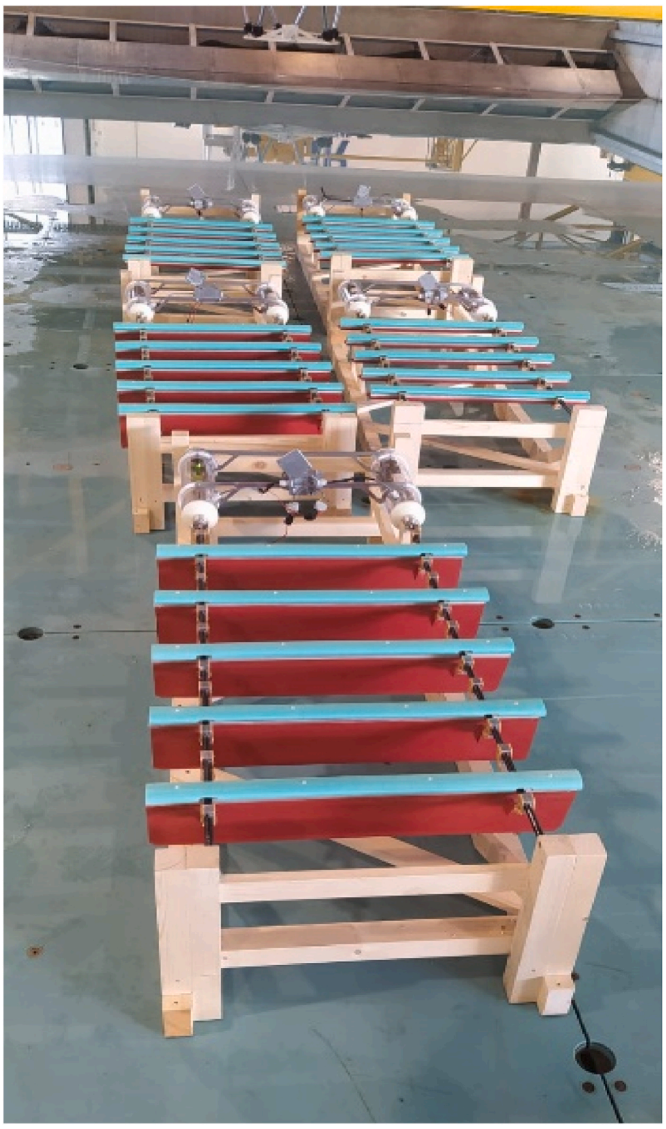

Fig. 6. Rear modules connected to the steering module.

wave period scale as: $\sqrt{\lambda} = \frac{T_p}{T_m}$. Therefore, the equivalent full-scale wave periods presented in Table 5 were obtained by multiplying the model-scale wave periods by $\sqrt{20}$. The same scaling approach was used only to provide full-scale interpretation of the tested wave conditions; the experimental results are presented at model scale for consistency with the numerical simulations.

4. Numerical modelling

4.1. Overview

The hydrodynamic behavior of the proposed system is simulated using OrcaFlex (Orcina, 2025), which solves the time-domain equations of motion for multi-body systems subjected to wave loading. The model implements the drag-based propulsion mechanism described in Section 2 by solving the time-domain problem using the Morison equation. The second-order wave effects such as Stokes drift, scattering, and radiation are not considered. However, these nonlinear effects are indirectly accounted for using the calibration factor, C_N^*. Simulations are performed under regular waves conditions corresponding to those used in the experimental programme. Each structural component (floaters and fins) is modelled using 6D buoy objects, which allow full rigid-body motion with six degrees of freedom. All hydrodynamic and inertial properties are defined at the object centre of gravity (CG), consistent with the OrcaFlex 6D buoy formulation.

4.2. OrcaFlex model

4.2.1. Object hierarchy and single-module configuration

Fig. 8 illustrates the OrcaFlex object hierarchy for a single float-fin module, the repeating unit of the full model. Each module comprises three objects connected in a parent child chain: a float 6D buoy (Parent 1), a constraint object representing the hinge, and a fin 6D buoy (Child 2) following the OrcaFlex constraint formulation.

The float 6D buoy is assigned the physical mass, displaced volume, waterplane area, and centre of gravity of the surface float, with its local axes x_{float} & z_{float} aligned with the global surge and heave directions respectively. The constraint object implements a pin joint: all relative translations and rotations between float and fin are suppressed except rotation about the local Y-axis (RY), which is the sole permitted degree of freedom. The constraint object defines both in-frame (rigidly attached to the float – Child 1) and an out-frame (reference frame for the fin – Parent 2), with local axes x_{hinge} & z_{hinge} in the plane of fin rotation. The stopper mechanism is implemented as a torsional spring-damper on the RY degree of freedom, activating at the prescribed limit angle. Forward and backward propulsion modes are implemented by reversing the direction of the RY angular limit, with no modification to any hydrodynamic parameter. The fin 6D buoy (Child 2) carries its own body-fixed local axes x_{fin} & z_{fin}, which rotate with the fin between its active (located at β) and feathered positions. Morison drag forces are applied independently in these local axes at each time step.

Table 3
Load cell calibration errors.

Load cell number	L1	L2
Maximum error	0.88%	0.75%

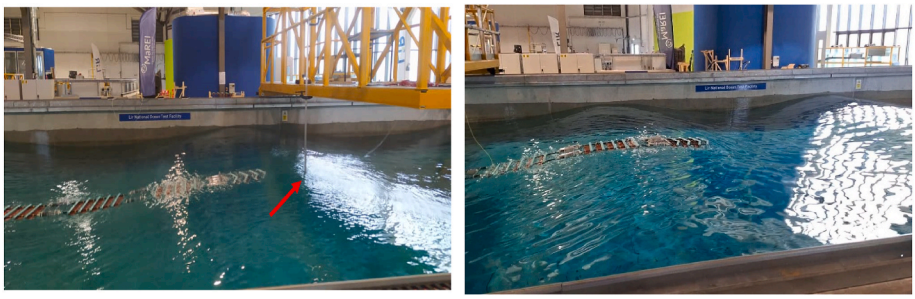

Fig. 7. Stationary (left) and nonstationary (right) setup used to measure the pulling capacity and velocity.

Table 4
Wave gauges calibration errors.

Wave gauge number	WG1	WG2	WG3	WG4	WG5	WG6	WG7
Calibration error	1.36%	0.23%	0.31%	0.66%	0.60%	0.27%	0.18%

Table 5
Wave characteristics at full and model scales.

Name	Full scale		Model scale	
	H [m]	T [s]	H [m]	T [s]
Reg1	4	10	0.2	2.236
Reg2	4	6	0.2	1.342
Reg3	4	8	0.2	1.789
Reg4	4	12	0.2	2.683
Reg5	4	14	0.2	3.130
Reg6	8	10	0.4	2.236
Reg7	8	6	0.4	1.342
Reg8	8	8	0.4	1.789
Reg9	8	12	0.4	2.683
Reg10	8	14	0.4	3.130

Table 6
Fin angles.

Fin direction	Fin angle
Forwards	*45°*
Forwards	*90°*
Backwards	*45°*
Backwards	*90°*

4.2.2. *Multi-module assembly*

Figs. 9 and 10 show the two rear modules in the side-view wireframe and three-dimensional render respectively. The global coordinate system follows the OrcaFlex convention (Orcina, 2025). Global Z points vertically upward, global X points from left to right, and the origin is at the mean still water level. In the wireframe, float 6D buoys appear as yellow square symbols at the waterline and fin 6D buoys as red cross symbols at the fin centroids below. The local hinge axis triads are visible at each module connection, confirming consistent RY orientation across all modules. There is an inter-module constraint connecting two modules shown at the centre which also has free RY along with appropriate rotational stiffness rather than being left entirely free or entirely rigid. The stiffness value is selected to be sufficiently high to maintain structural coherence of the assembly under wave loading, preventing unrealistic relative angular displacement between modules, while remaining low enough to ensure the multi-module system behaves as a flexible, non-monolithic structure rather than a single rigid body. Similarly, the rotational stiffness for the stopper is chosen through a sensitivity study and comparison with the experimental data with higher stiffness used to arrest fins rotation.

4.2.3. *Plan view and module arrangement*

Fig. 11 shows the plan view (global X-Y plane) of the complete model, comprising four rear propulsion modules and one forward

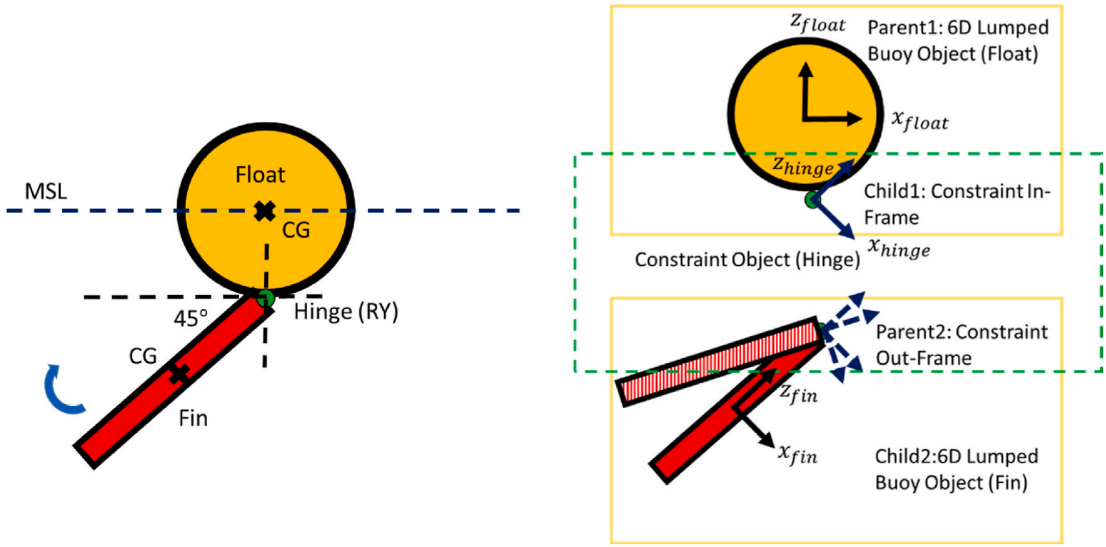

Fig. 8. OrcaFlex single float-fin object hierarchy.

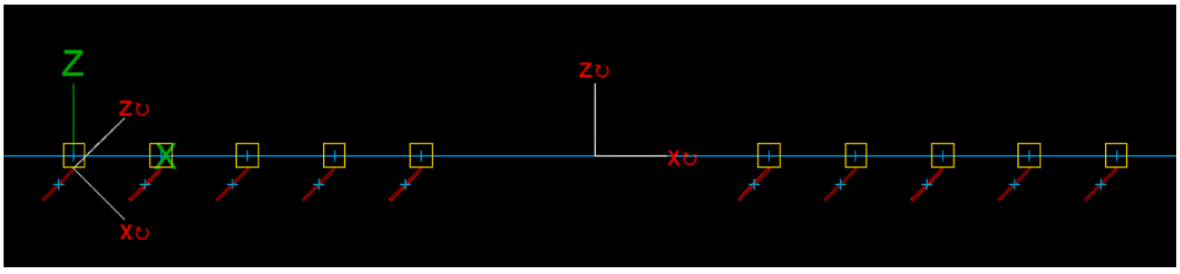

Fig. 9. Side-view wireframe of two modules showcasing global axes, float-fin hinge and inter-module hinge axes.

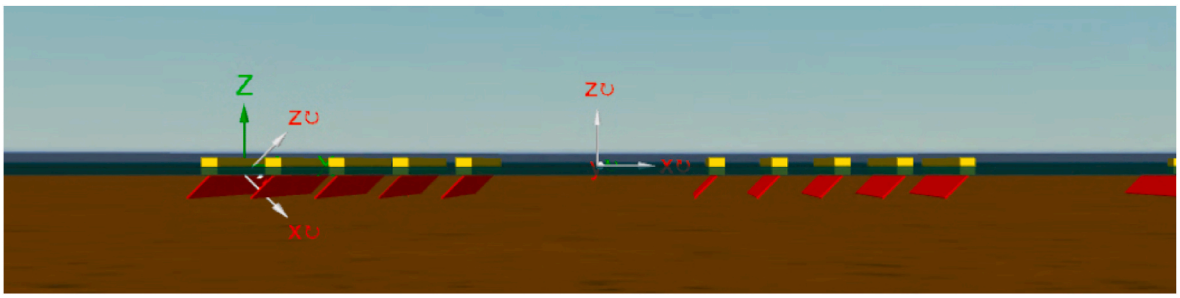

Fig. 10. Side-view 3D render of two modules.

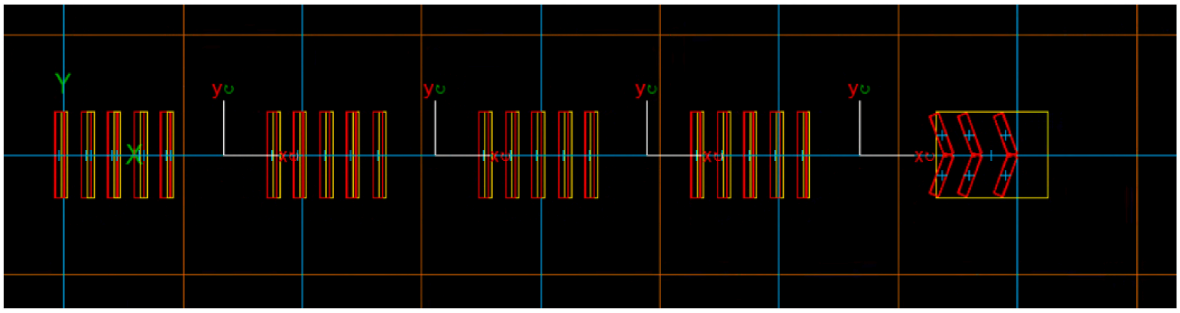

Fig. 11. Plan view of USV wireframe model.

steering module. Rear module fin buoys appear as spanwise-aligned clusters, confirming that the fin span is oriented in the global Y-direction and that all fins within a module share the same longitudinal position. The steering module fins are oriented differently in plan, reflecting the modified angular constraint that generates a transverse force component for directional control.

5. Results and discussion

5.1. Experimental results

The effects of fin angles/direction, wave condition and number of modules on the device pulling capacity and velocity were examined. It is noted that all the results are presented in model scale.

5.1.1. Fin angle effect

- Movement in the wave propagation direction:

  Two fin angles were tested during the experimental campaign, including 45° and 90° in forward and backward directions (See Fig. 3 for forward and backward definition). The forward angle resulted in a movement in the direction of wave propagation, whereas the backward fin angle caused movement opposite to the wave propagation direction. The results show that higher velocity and average pulling capacity are obtained at 45°. Regarding the average pulling capacity which is shown in Fig. 12, the largest difference occurs for a wave period of 1.342s, where a 30% difference can be detected in the pulling capacity of the model. However, longer wave periods show a convergence and reduction in the magnitudes of both parameters. The reason why longer wave periods can cause lower velocity or pulling capacity is due to the fact that shorter wave periods have

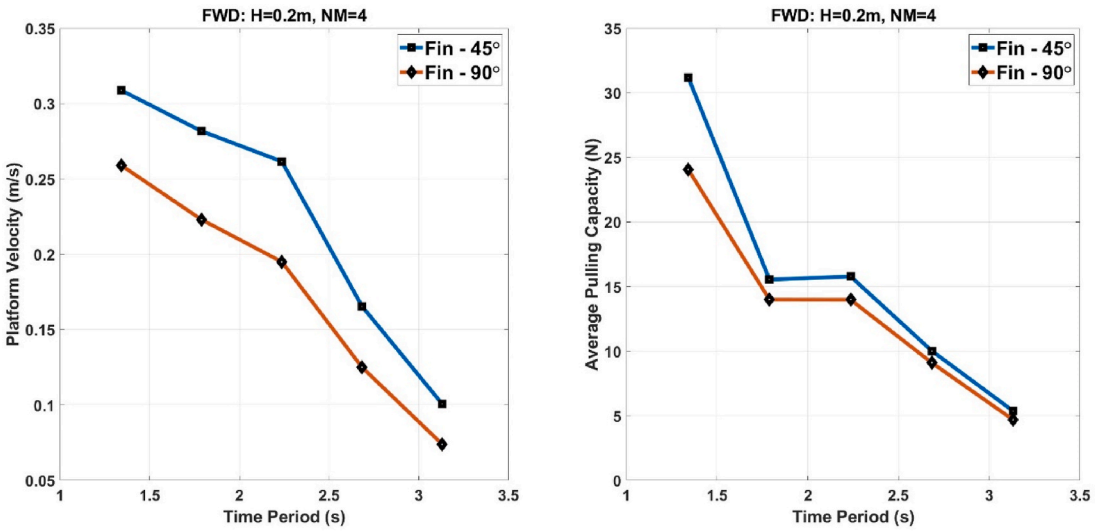

Fig. 12. Velocity and average pulling capacity of the device against wave period at wave height of 0.2 m and 4 module numbers for two forward fin angles.

larger orbital velocities and accelerations (Table 1). In addition to that, shorter wave periods result in more frequent and rapid wave cycles, providing more opportunities for the device to capture and convert the wave energy into forward motion.

- Movement opposite to the wave propagation direction:

  The device performance with 45° and 90° backward fin angles is shown in Fig. 13. In this case, the trend of velocity and pulling capacity changed in such a way that the highest velocity and pulling capacity are obtained at 2.236s and 1.788s wave periods, respectively. The results again confirm that better performance can be obtained at 45° rather than 90° fin angle. The 45° fin angle strikes a better balance between capturing sufficient wave energy during fins oscillation and releasing it to propel the device forward. This balance could be critical for achieving higher velocities.

In comparison to forward fin angle, even though the device can move against the wave propagation direction, its performance is lower than the opposite direction of movement. It is also worth mentioning that contrary to the forward fin angle, at 1.342s wave period, no surge movement was detected, showing that the device does not move at wave periods $\leq$1.342s. This can be attributed to the Stokes drift phenomenon. When the model moves against the wave propagation direction it must overcome the velocity induced by Stokes drift. The effect of Stokes drift is more significant at shorter periods such as 1.342s and 1.788s. This explains why the model velocity and pulling capacity decrease when it moves opposite to the wave propagation direction.

For wave periods larger than 2.236s, the trend of velocity and pulling capacity for this case follows the same trend as forward fin angle. In fact, when the effect of wave induced Stokes drift is decreased for wave periods larger than 2.236s, the orbital velocity of the wave would be the main reason for propelling the device. Therefore, due to the lower orbital velocities at longer wave periods the flapping motion of the fins and its effect on propelling the model opposite to the wave decreases and leads to lower velocity and pulling capacity.

Equation (13a) shows that horizontal thrust (surge) scales as $sin\,\beta$, which reaches its maximum value of unity at $\beta = 90°$ (a vertical fin). This might suggest that a vertical fin orientation is optimal. However, this conclusion neglects the critical role of the orbital velocity component capture, specifically, the dependence of $|V_{rel}|$ on β through the projected area of the fin relative to the flow direction. For a vertical fin with stopper at $\beta = 90°$, the fin face is parallel to the vertical orbital velocity and perpendicular to the horizontal orbital velocity. The fin therefore presents zero projected area to the vertical orbital velocity. The drag force in the Morison formulation acts entirely in the horizontal direction, capturing only the horizontal orbital velocity component. Since u_x and u_z are approximately equal in amplitude at the surface for a progressive wave, the vertical fin discards half of the available orbital kinetic energy.

For an inclined fin ($\beta = 45°$), the sin β projection factor is 0.707, reduced relative to the vertical fin by a factor of $1/\sqrt{2}$. However, the fin now presents balanced projected areas to both the horizontal and vertical orbital velocity components. The relative velocity magnitude, therefore, incorporates contributions from both u_x and u_z, recovering the orbital kinetic energy that the vertical fin discards. That is the reason why 45° fin outperformed 90° fin across the range of wave periods.

5.1.2. *Wave height effect*

In this section, the effect of wave height on the device's performance is evaluated. In addition to the 0.2 m wave height, the results of the 0.4 m wave height are presented to investigate the effect of wave height. All the parameters, including the fin angle and the number of modules, were kept unchanged. The fin angle was set at 45° forward which had already been shown to perform better. Four modules were used in all these tests.

The results indicate that the 0.4 m wave height led to higher velocities and pulling capacities in the device. Results show that the device has considerably better performance in shorter wave periods (less than 1.789s) especially when it comes to pulling capacity. Fig. 14 shows an increase of 65% to 140% in velocity due to the doubling of the wave height. In this regard, it is interesting that for larger wave periods (T $\geq$ 2.683s), the rate at which the model velocity changes is higher, and it is closer to the rate of change in their respective orbital velocities (See Table 1). Fig. 14 shows that, for a wave height of 0.4 m, the average pulling capacity of the device reaches 57.6 N and 17.2 N at wave periods of 1.342s and 3.130s.

5.1.3. *Number of modules*

The length or number of the modules' effect on the model performance is investigated in this section. The tests were performed for wave heights of 0.2 m and 0.4 m at 45° forward fin angle. The effect of module number is insignificant at wave height of 0.2 m (Fig. 15a and b). Unlike 0.2 m wave height, the effect of the number of the modules is more pronounced at wave height of 0.4 m (Fig. 15c and d). While the average pulling capacity follows the same trend for the four and five module number (Fig. 15c) the velocity of five module number indicates a decreasing trend at lower wave periods (T < 2.236s). The decreasing trend in velocity observed with the addition of a fifth module at lower wave periods (T < 2.236s) suggests a complex interplay between

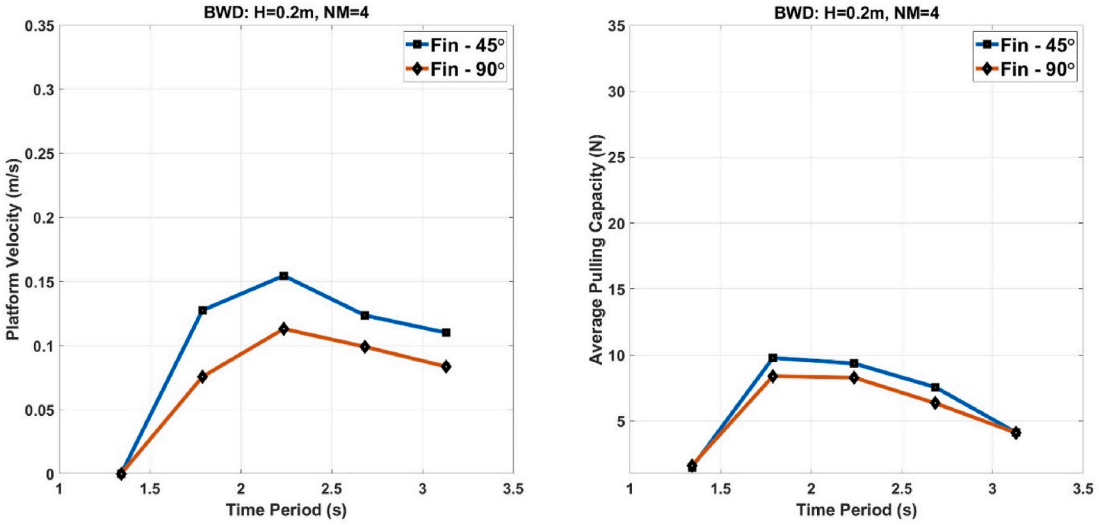

Fig. 13. Velocity and average pulling capacity of the device against wave period at wave height of 0.2 m and 4 module numbers for two backward fin angles.

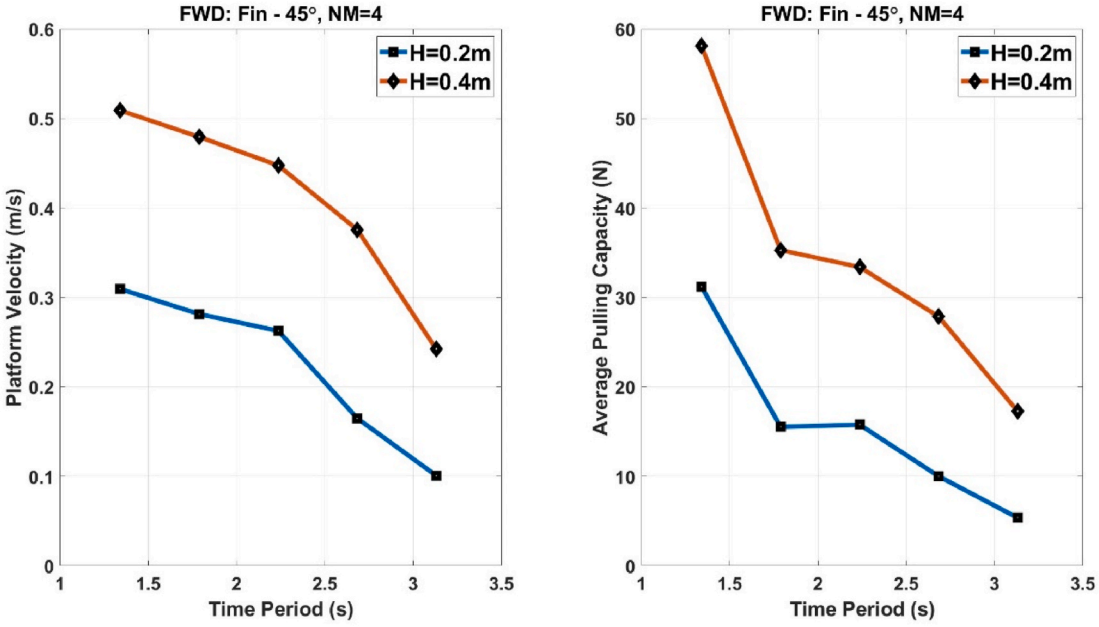

Fig. 14. Velocity and average pulling capacity of the device against wave period for 45 forward fin angle and four modules at wave height of 0.2 m and 0.4 m.

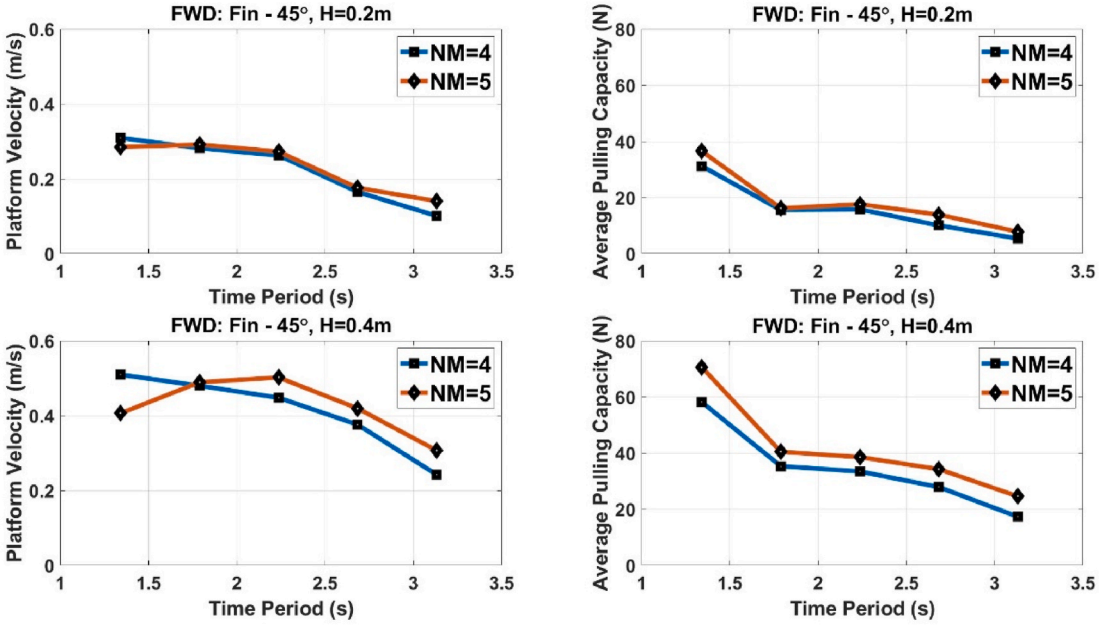

Fig. 15. Velocity and pulling capacity of the device against wave period at 45° forward fin angle and 0.2 m and 0.4 m wave height for two different module numbers ((a)-(d) are arranged clockwise from the top-left plot).

wavelength and device dynamics. This means that adding the fifth module reduces the forward propulsion force.

5.1.4. Model general performance

To have a better understanding of the model's general performance and in order to derive its performance in different wave conditions, the velocity and average pulling capacity are plotted against the nondimensional ratio lm/L (module length to wavelength) ratios regardless of the number of the modules. Therefore, the plots can be used for optimizing the design. According to Fig. 16, the same trend can be seen for both 0.2 m and 0.4 m wave heights. The only difference was the amount of velocity and pulling force, which was discussed in previous sections. The results suggest a linear behavior of the model. It is also notable that the minimum length of the module should be at least one wavelength to obtain 0.27 m/s velocity and 16 N pulling capacity for 0.2 m wave height. However, to get better performance, a module length to wavelength ratio (lm/L) larger than 1.5 improves the pulling capacity significantly. For lm/L larger than 1.5, the velocity of the device does not vary significantly. This behavior is due to the larger impulse force exerted by shorter periods. In addition to that, the acceleration variation rate is larger than the velocity variation in short period waves. It accounts for the significant variation in pulling capacity for larger lm/L.

5.1.5. Model optimization

To enhance the performance of the model, an initial optimization was conducted by modifying the fin spacing. Specifically, the fin

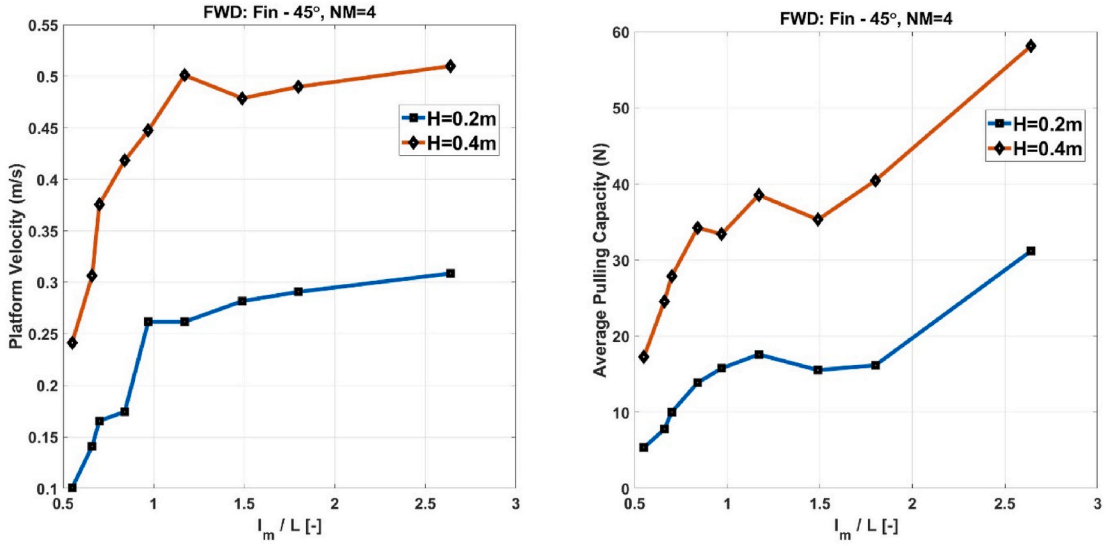

Fig. 16. Velocity and average pulling capacity of the device against lm/L ratio at 45 forward fin angle and 0.2 m and 0.4 m wave height conditions.

distance was reduced from 20 cm to 15 cm in two of the four modules, while the original spacing was maintained in the remaining two modules. The modified module is shown in Fig. 17. This modification increased the number of fins in the adjusted modules from 5 to 7 and added the control boxes on top of the module to decrease the length of the model by approximately 25%.

The results of this optimization demonstrate a notable improvement in both the velocity and the pulling capacity of the device, highlighting the effectiveness of fin spacing as a key parameter. It is noted that these tests on optimized model were conducted just for a limited set of sea states and a 45° forward fin angle. The velocity analysis shows a significant improvement where the optimized model velocity increased more than doubled at all investigated wave periods (Fig. 18). The results also indicate that 0.1 m wave height for optimized model led to higher velocities than 0.2 m wave height for configuration 1 (default model). Similar results were obtained for average pulling capacity. The optimized model shows higher pulling capacity even with lower wave heights (Fig. 19). It should be highlighted that the pulling capacities reported here are all average values. The maximum pulling capacity in different wave periods is much higher than average values and reaches 210 N for 0.2 m wave height and 2.683s wave period.

5.1.6. Uncertainty analysis

Uncertainty analysis is an essential component of experimental studies because the true value of a measured quantity cannot be known exactly. Its purpose is to estimate a reasonable range within which the true value is expected to lie at a specified confidence level. In the present study, uncertainty was evaluated in accordance with the recommendations of the International Towing Tank Conference (ITTC,). Two main sources of uncertainty were considered: Type A and Type B. Type An uncertainty was determined from the statistical analysis of repeated measurements, whereas Type B uncertainty was estimated from sensor calibration data, previous experience, and manufacturer specifications. Further details of these procedures are provided in (ITTC, 2024 ; Judge et al., 2021; Zabihi et al., 2019). The combined standard uncertainty may then be obtained by applying the root-sum-square combination of the Type A and Type B components.

The uncertainty analysis was conducted for five representative test conditions corresponding to the 45° fin configuration. Although ITTC guidance generally recommends a larger number of repetitions, typically around ten, the representative tests were repeated three to five times in the current study due to time and operational limitations associated with wave-tank testing. Nevertheless, the available repeated tests provided a reasonable basis for estimating experimental repeatability. The corresponding uncertainty results are presented in Table 7. As shown in Table 7, the combined standard uncertainty ranged from 1.35% to 1.66% across the investigated cases. The pulling-capacity measurements exhibited combined uncertainties of 1.58% and 1.35%, while the corresponding values for velocity ranged from 1.36% to 1.66%. The Type B contribution to the velocity uncertainty was comparatively small, indicating that the combined uncertainty was dominated primarily by the variation between repeated tests.

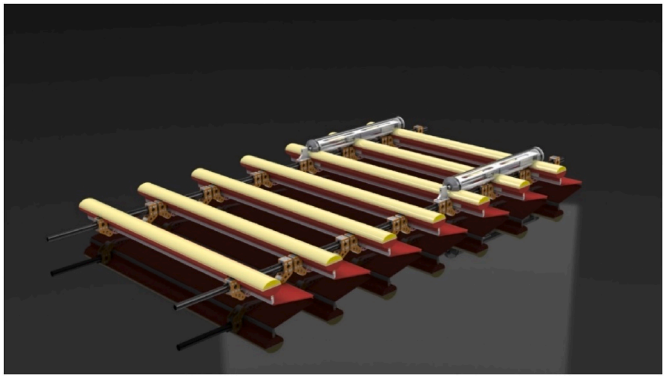

Fig. 17. Modified module with 7 fins instead of 5.

5.2. Numerical model output

This section presents the results obtained from the equivalent numerical model, together with the validation of experimental surge velocities for both forward and backward propulsion modes. The underlying propulsion physics, including wave-particle motion, passive fin rotation and stopper engagement are also explained in this section. In addition, the effect of fin inclination angle on performance is investigated, extending the range of conditions examined in the experiments.

5.2.1. Model validation

Fig. 20 presents the comparison between experimental measurements and numerical predictions for the 45° fin configuration in both forward and backward propulsion modes across the full range of wave periods tested. The effective drag coefficient C_N^* was calibrated independently for each wave period and propulsion mode, ensuring the model is optimally tuned at each condition. In the backward mode,

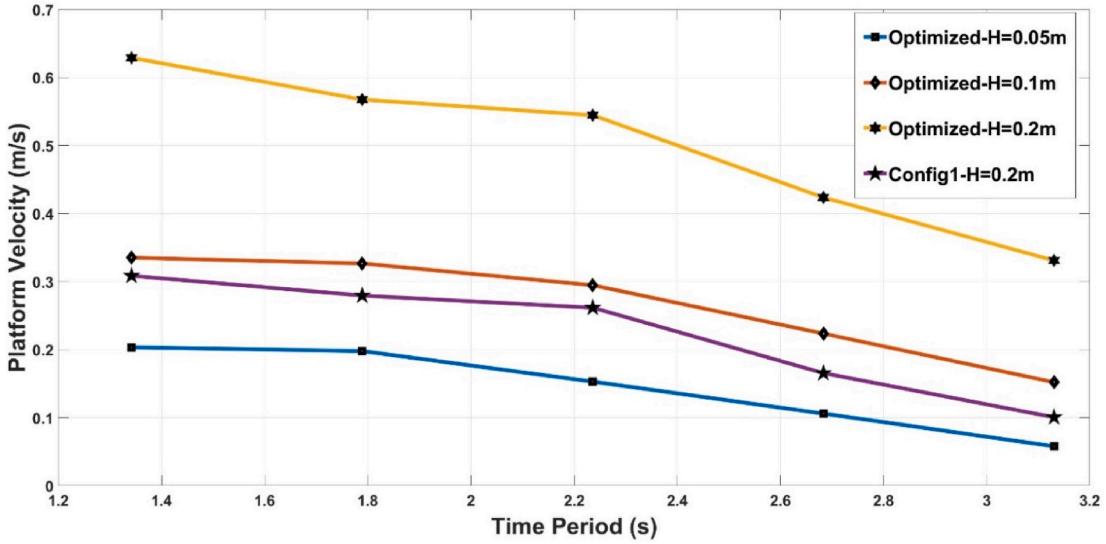

Fig. 18. Comparison of the velocity of the device against the wave period for optimized model and configuration 1.

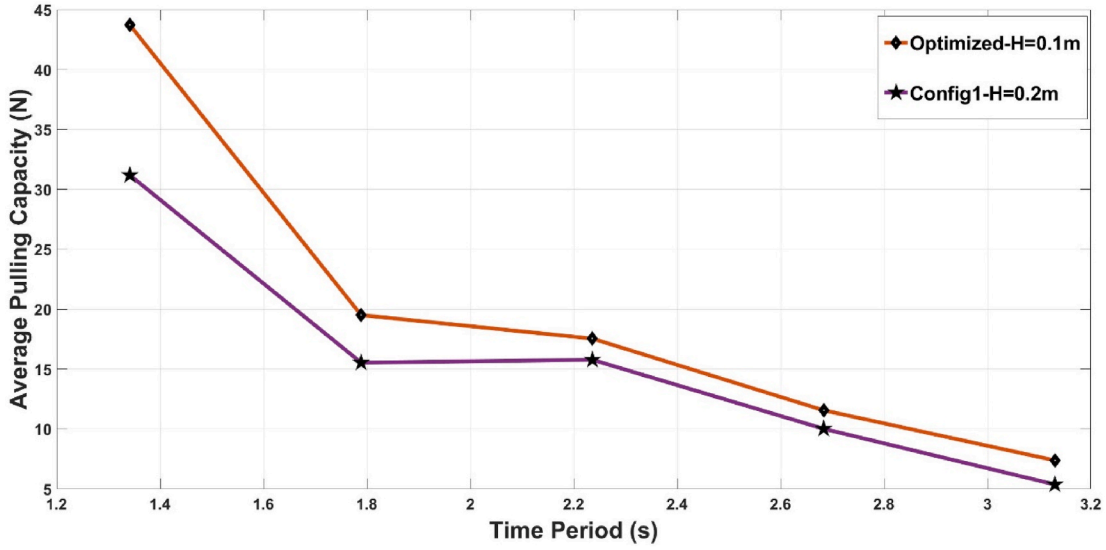

Fig. 19. Comparison of the average pulling capacity of the device against the wave period for optimized model and configuration 1.

Table 7
Uncertainty Analysis for five representative cases.

Test case	Configuration	Target Wave Condition	Measured parameter	Mean value of repeated tests	u_A [%]	u_B [%]	u_S [%]
U1	FWD, NM = 5, Fin45 °	H = 0.2 m,T = 1.342s	Pulling capacity	36.48 N	1.31	0.88	1.58
U2	FWD, NM = 5, Fin45 °	H = 0.2 m,T = 3.130s	Pulling capacity	7.76 N	1.03	0.88	1.35
U3	FWD, NM = 4, Fin45 °	H = 0.4 m,T = 1.342s	Velocity	0.51 m/s	1.39	0.02	1.39
U4	FWD, NM = 4, Fin45 °	H = 0.4 m,T = 2.236s	Velocity	0.45 m/s	1.66	0.024	1.66
U5	BWD, NM = 4, Fin45 °	H = 0.2 m,T = 2.683s	Velocity	0.12 m/s	1.36	0.088	1.36

agreement is good across all periods, with both curves capturing the characteristic non-monotonic response: near-zero velocity at T = 1.342s, a peak at T = 2.236s, and a gradual decline beyond. In the forward mode, agreement is satisfactory at shorter periods, but the numerical model underpredicts at T = 2.236s. Since C_N^* is calibrated at each condition, this divergence is not attributable to coefficient mismatch. Overall, the model successfully reproduces the key physical trends in both modes: the monotonically decreasing forward velocity, the non-monotonic backward response, and the velocity asymmetry between modes confirming that the Morison-based 6D buoy framework provides a physically sound representation of the USV propulsion mechanism within the validated wave period range.

5.2.2. *Stopper effect outcome – backward mode*

The physical basis of thrust generation in the wave-propelled USV is illustrated through four synchronized time histories extracted from the OrcaFlex numerical model for fin 16 operating in the backward propulsion mode: the local sea surface elevation at the fin location (Figs. 21a and 22a), the surge connection force at the hinge (Figs. 21b and 22b), the fin pitch angle (Figs. 21c and 22c), and the fin surge

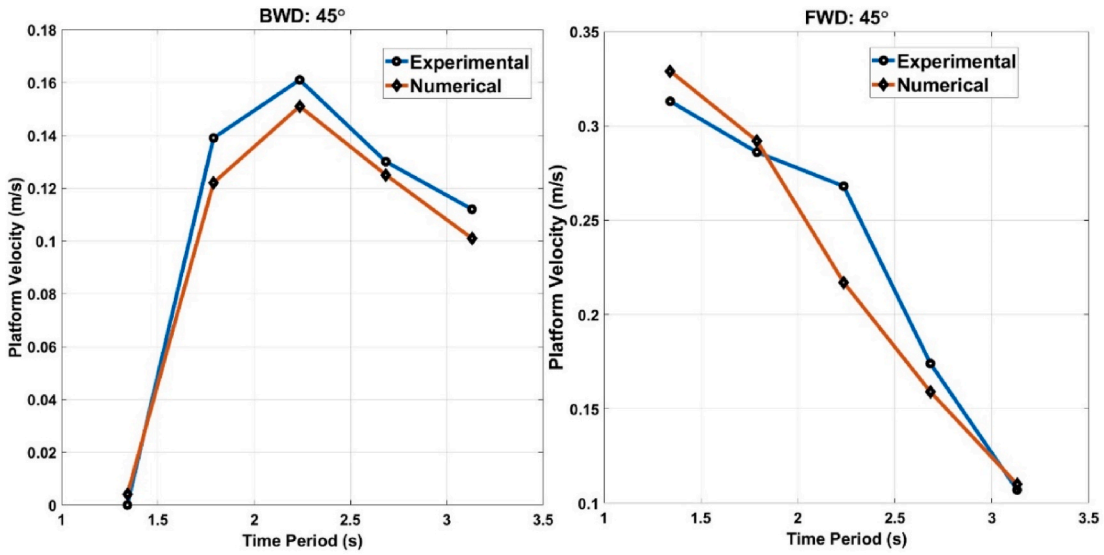

Fig. 20. Comparison of experimental and numerical velocities for backward (left) and forward (right) modes.

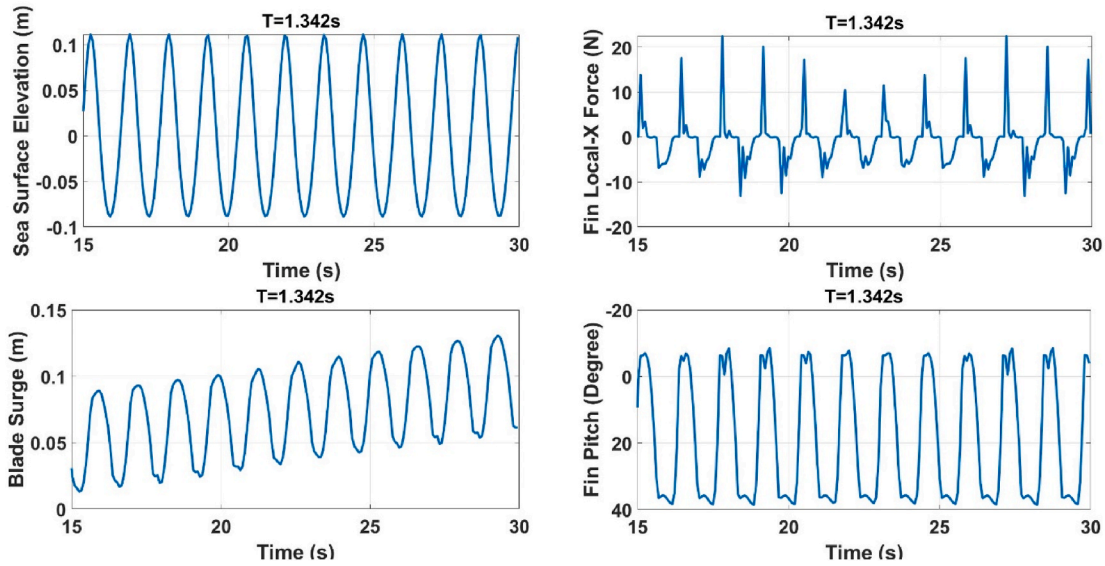

Fig. 21. Stopper effect for T = 1.342s in backward USV mode ((a)-(d) are arranged clockwise from the top-left plot).

position (Figs. 21d and 22d), for wave periods T = 1.342s and T = 2.236s, corresponding to full scale periods of T = 6s and T = 10s, respectively.

The sea surface elevation (Figs. 21a and 22a) provides the wave phase reference for the subsequent panels. The signal is sinusoidal with amplitude approximately [H/2] at the fin location, oscillating at the incident wave frequency (See Fig. 23). The crest corresponds to wave phase $\theta = 0$ and the trough to $\theta = \pi$ in the orbital velocity convention of Equations (3) and (5), establishing the phase relationships required to interpret the force and motion responses below.

Considering the time instant $t \approx 21.2$s as a representative reference identifiable in Fig. 21a as the trough of the surface elevation, fin 16 is at its lowest wave phase position, where the local vertical particle acceleration ($a_z > 0$ *at* $\theta = \pi$) dominates. This generates a hydrodynamic moment which drives the fin toward the stopper limit. Once engaged, the fin is held rigid at $\beta = 45°$ and a reaction force is applied at the hinge, visible as the negative force spikes in Figs. 21b and 22b occurring precisely in phase with the surface elevation trough. The negative sign of the connection force represents the stopper reaction; by Newton's third law, the equal and opposite force transmitted to the USV constitutes a net positive thrust in the backward propulsion direction. The correspondence between the trough of Fig. 21a and the negative force spike of Fig. 21b confirms that thrust is generated exclusively at the wave trough phase, consistent with the half-cycle rectification mechanism of Section 2.1.

Conversely, at the wave crest ($\theta = 0$, identifiable as the positive peaks of Figs. 21a and 22a), the vertical particle velocity is directed downwards, $u_z < 0$). This acts on the back face of the fin with no stopper present on this side and the fin rotates freely to the feathered position.

The four-panel synchronization: trough (a) → negative force spike in (b) → flat top (stopper engaged) in (c) → small forward step in (d); crest (a) → positive force in (b) → rapid rotation in (no stopper) (c) → position recovery in (d) constitutes direct numerical evidence of the complete stopper rectification cycle described theoretically in Section 2.1.

The local x-axis translation (local surge of the fin) time histories of fin 16 for T = 1.342s and T = 2.236s (Figs. 21d and 22d respectively) provide direct visualization of the half-cycle rectification mechanism and its dependence on wave period. At T = 2.236s (Fig. 22d), the surge

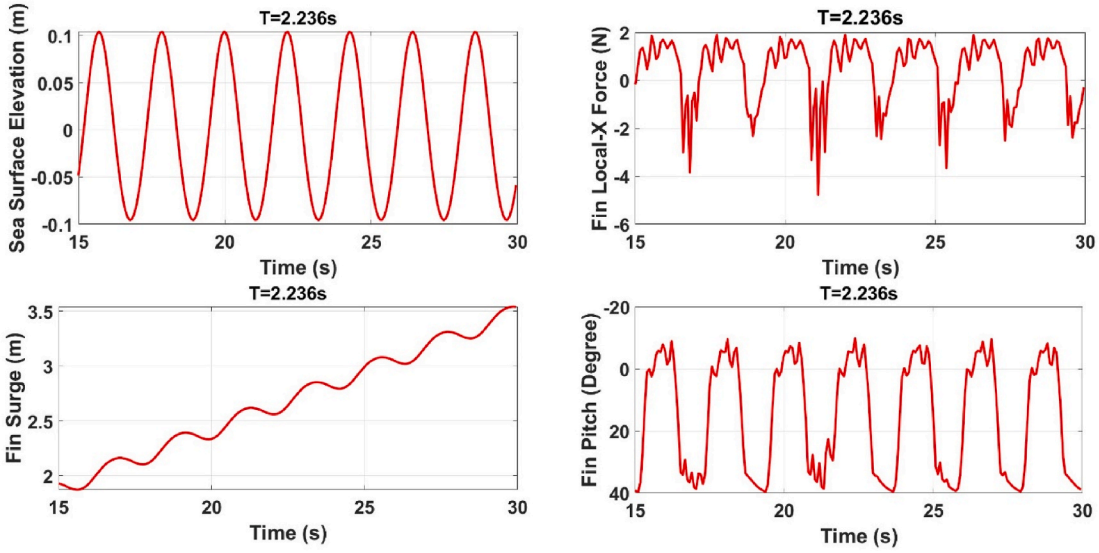

Fig. 22. Stopper effect for T = 2.236s in backward USV mode (a-d is from top-left plot in clockwise direction).

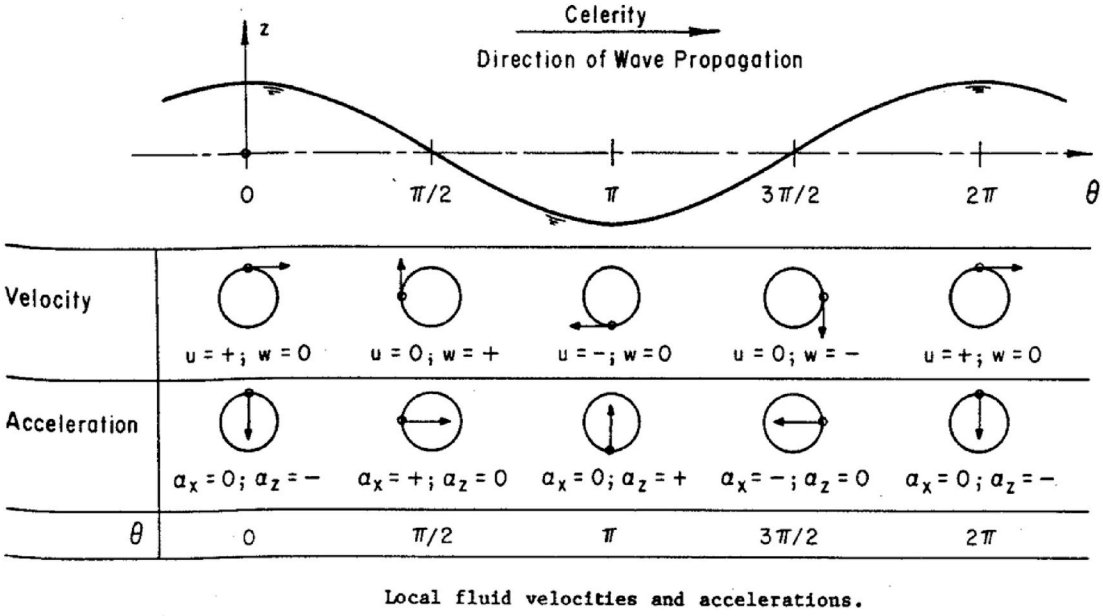

Fig. 23. Wave particle velocities and accelerations-adopted from (Shore Protection Manual, 1984).

displacement exhibits a characteristic staircase pattern: a positive surge increment during the trough phase when the stopper is engaged and backward thrust is generated followed by a plateau during the crest phase when the fin is lifted with the wave and net surge advance is suppressed. Each step corresponds to one wave cycle and the cumulative ramp, yielding a mean surge velocity of approximately 0.151 m/s at model scale, is direct numerical evidence of the nonlinear drag rectification mechanism described in Section 2.1.

At T = 1.342s (Fig. 21d), the behavior is qualitatively different: the local surge displacement oscillates about a nearly stationary mean with increasing amplitude, showing no sustained directional progression. This arises primarily from spatial phase incoherence between modules at shorter wavelengths. Adjacent modules experience different wave phases simultaneously while some modules at the trough generate thrust, neighboring modules at the crest undergo opposing forces, resulting in a push–pull interaction that cancels net advance and leads to oscillatory motion rather than steady propulsion. Fig. 24 shows the graphical view from the OrcaFlex simulation demonstrating the propulsion phenomenon visually.

Fig. 25 shows the module-level average force vectors (blue) and the global resultant force (red) for backward mode at $T = 1.342$ s (left) and $T = 2.236$s (right). Each vector M_i represents the average force of the five fins within a module, while the red vector denotes the resultant obtained by summing all module contributions.

At $T = 1.342$ s (left), the resultant force has a magnitude of approximately 20.46 N and is oriented at about 86.4°, indicating that the force is predominantly vertical. The horizontal component (surge-driving component) is therefore small, while the vertical component dominates. This implies that most of the hydrodynamic loading is associated with oscillatory heave-type motion rather than propulsion. The spread of module vectors across different directions further indicates phase incoherence, leading to partial cancellation in the surge direction and resulting in a push–pull oscillatory behavior with negligible net advance.

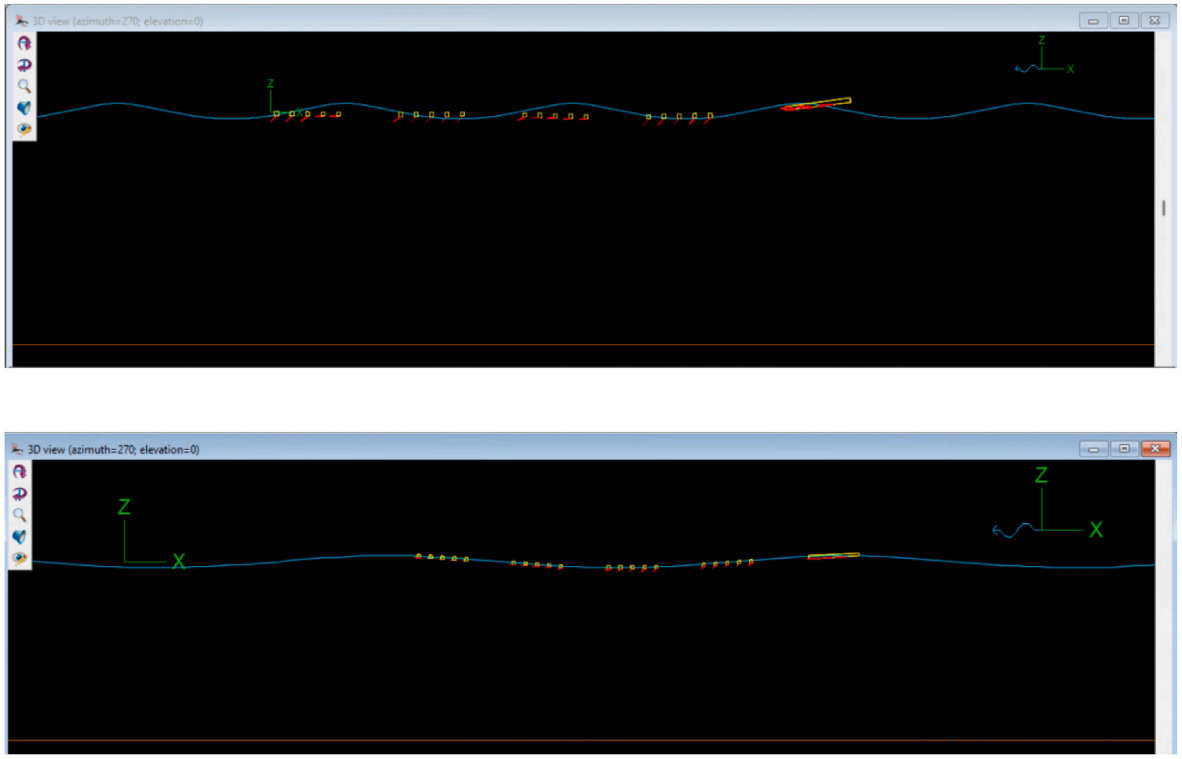

Fig. 24. OrcaFlex 3D side-view snapshot of the USV in backward propulsion mode (T = 1.342s top, T = 2.236s, bottom).

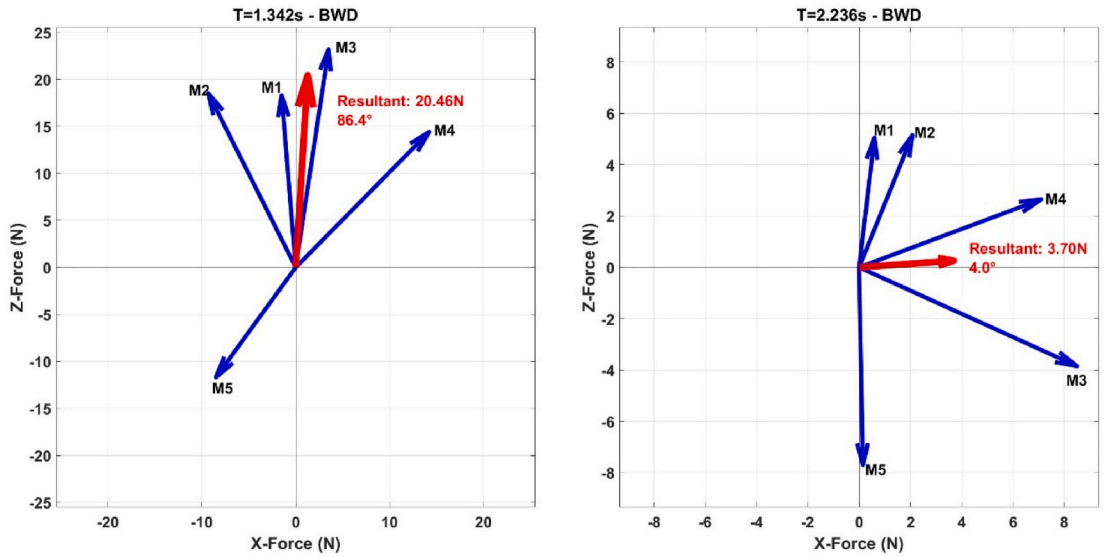

Fig. 25. Module wise average and resultant force for backward mode at T = 1.342s and T = 2.236s.

In contrast, at $T = 2.236$ s (right), the resultant force is approximately 3.70 N and is oriented at about 4.0°, indicating strong alignment with the horizontal direction. The horizontal component of the resultant is therefore significantly larger relative to the vertical component (approximately 3.5–3.7 N in surge), while the vertical contribution is minimal. This demonstrates that the forces generated by different modules are more coherently aligned in the surge direction, leading to effective propulsion.

Despite the smaller total force magnitude at $T = 2.236$ s, the greater horizontal alignment of the resultant force results in improved conversion of wave-induced forces into surge motion, and hence higher velocity. Conversely, at $T = 1.342$ s, the dominance of the vertical component leads to inefficient propulsion and oscillatory motion.

5.2.3. *Stopper effect outcome – forward mode*

Unlike the backward mode, in the forward mode, at T = 1.342s (See Fig. 26), the thrust is generated when the wave surface elevation is in the vicinity of the mean level ($\theta = \pi/2$ or $3\pi/2$). At this phase, the horizontal particle acceleration reaches maximum in the direction of wave propagation while the vertical particle acceleration is zero. This drives the fin to its stopper limit, generating the thrust. In contrast, when at crest and trough, the fin freely rotates between 0° and 45°, producing no thrust as observed in Fig. 26.

Interestingly, at T = 2.236s, the generation of thrust is at the crest of

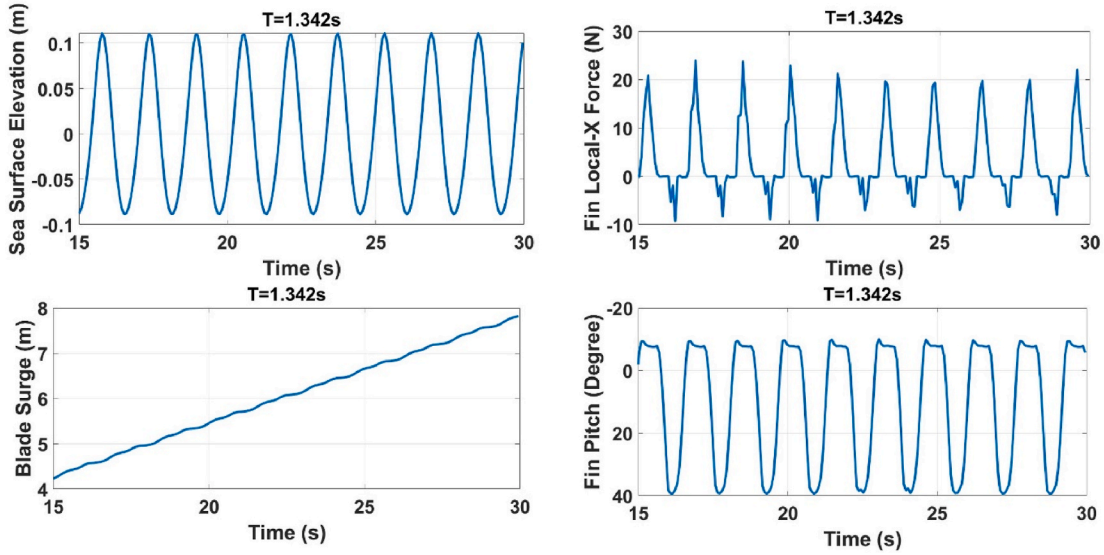

Fig. 26. Stopper effect for T = 1.342s in forward USV mode (a-d is from top-left plot in clockwise direction).

the wave surface where the vertical particle acceleration is maximum ($a_z < 0$) as shown in Fig. 27. At trough, the surge plateaus clearly where the fin is feathering freely without any stopper engagement.

5.2.4. Effect of fin inclination angle

The experimental program examined two fin inclination angles, 45° and 90°. To broaden the parameter space, additional numerical simulations were performed for inclination angles of 22.5° and 67.5°. All other model parameters were kept consistent with those of the corresponding validated experimental cases. These supplementary simulations enable a more comprehensive sensitivity analysis of the effect of fin inclination across the investigated wave period range.

Fig. 28 presents the model velocity in the backward propulsion mode. The 45° fin configuration consistently yielded the highest velocities across the investigated wave periods, with a peak response observed at $T = 2.236$ s. The remaining inclination angles exhibited a similar period-dependent trend; however, they generally produced lower velocities. These findings suggest that a 45° inclination provides a favorable balance between projected area and effective horizontal force generation for backward propulsion under the present conditions.

The corresponding forward propulsion results are shown in Fig. 29. At the shorter wave periods, the 22.5° fin produced the highest velocities, followed by the 45° configuration. As the period increased, the differences between the 45°, 67.5° and 90° configurations diminished, whereas the performance of the 22.5° configuration decreased more rapidly. This behavior indicates that the influence of fin inclination is strongly coupled with both the incident wave period and the direction of propulsion.

Considering both forward and backward propulsion over the full range of investigated wave periods, the 45° configuration demonstrated the most robust and consistent overall performance. It achieved the highest velocities in backward propulsion while maintaining comparatively strong performance in forward propulsion. However, a more comprehensive optimization study encompassing a wider range of inclination angles, wave heights, irregular sea states, and geometric parameters would be necessary to establish generalized design recommendations.

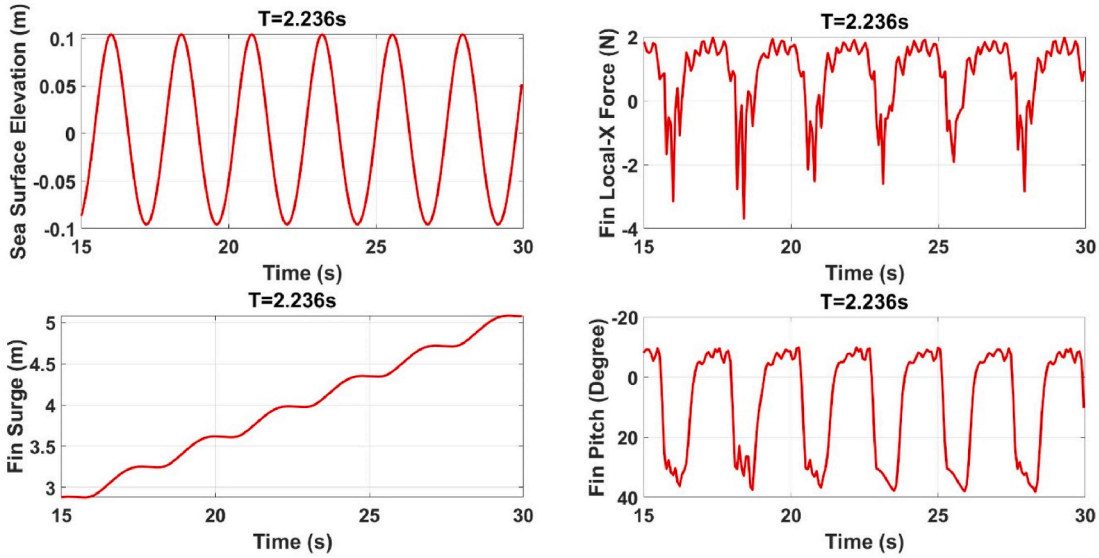

Fig. 27. Stopper effect for T = 2.236s in forward USV mode (a-d is from top-left plot in clockwise direction).

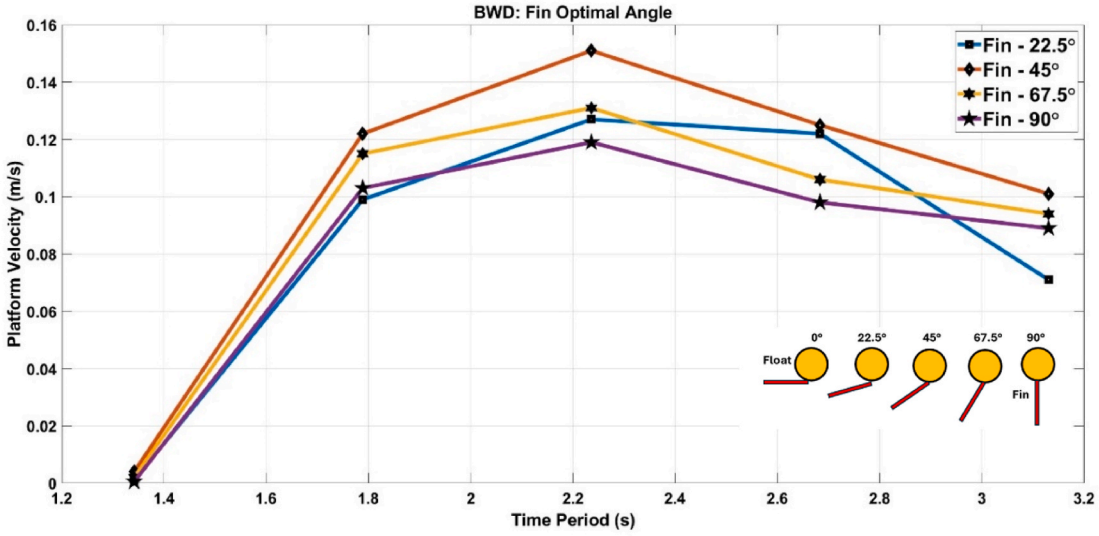

Fig. 28. Backward propulsion velocity for fin inclination angles of 22.5°, 45°, 67.5° and 90°.

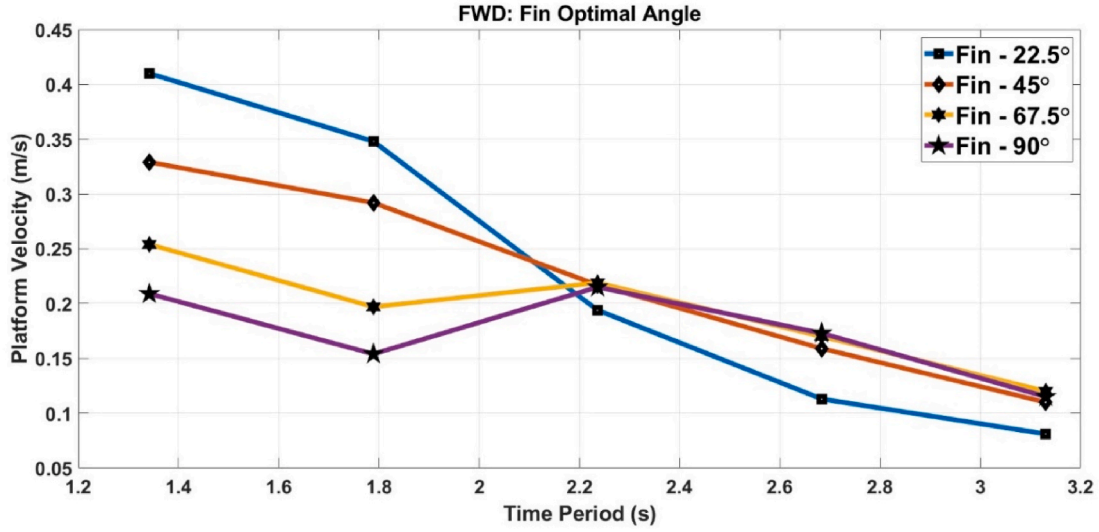

Fig. 29. Forward propulsion velocity for fin inclination angles of 22.5°, 45°, 67.5° and 90°.

6. Conclusion

This paper introduces a new concept of wave-powered unmanned surface vehicles called OR-CA. The system features a surface-piercing float connected to submerged fin assemblies through struts, with each fin pivot-mounted and limited to a maximum angle by a mechanical stopper. Under wave action, fluid orbital motion interacts with the inclined fins, generating a net hydrodynamic force that drives the vehicle forward or backward. The present study focused on establishing the physical basis of wave-driven propulsion through nonlinear drag rectification and validating the concept using a combined experimental and numerical approach.

The device has successfully shown its ability to move in different directions with energy extracted from the waves. The key results are summarized as follows.

- Among the four fin angles (22.5°, 45°, 67.5°, and 90°) studied, the 45° configuration demonstrated the most robust and consistent overall performance.
- The model performs better in short period waves (T = 1.342s) if the fins' angles are set in the forward direction. When the fins' angles are set in the backward direction, the model stops moving at T = 1.342s. For the backward fin angle (moving against the wave propagation direction), the highest velocity and pulling capacity are obtained at T = 2.236s and T = 1.789s, respectively.
- Increasing wave height improves the model's performance. The results show that doubling the wave height increases the velocity by 65% to 140% and the pulling capacity by 86% to 220% depending on the wave period.
- Based on the general trends of the device performance obtained at different ratios of module length to wavelength (lm/L), the minimum ratio of 1 is recommended. It should be kept in mind that larger lm/L could significantly improve the device pulling capacity for the forward fin orientation (moving along the wave propagation direction); however, the velocity plateaus for lm/L larger than 1.5.
- Decreasing the spacing between the fins in two of the modules and having 7 fins instead of 5 significantly improved the velocity and pulling capacity of the device so that better results were obtained with halved wave heights.

- The validated numerical model confirmed that the propulsion mechanism of the USV is governed by stopper engagement, which breaks the symmetry of fin motion.

Although the tests were preliminary, they do indicate that the OR-CA concept has the potential to operate as a USV. The numerical model employs a Morison-type formulation with an effective drag (rectification) coefficient and does not explicitly resolve higher-order nonlinear wave–structure interactions, viscous flow separation, wave drift, or blade–blade shielding effects. Similarly, the experimental measurements are limited to global performance metrics (surge velocity and pulling capacity) under different sea states and fin angles and do not directly capture local hydrodynamic force distributions or unsteady flow features. Future work will focus on improving the fidelity of the numerical model by incorporating detailed hydrodynamic interactions, including shielding effects between blades, fully nonlinear wave–structure coupling, and potentially CFD-based force modelling. These developments will enable a more accurate prediction of local forces and energy transfer mechanisms and provide a rigorous comparison with the present rectification-based Morison approach. Such studies will also support optimization of geometry and layout for improved propulsion efficiency before the next tank testing campaign. Future work should also characterise the performance of the OR-CA system in more realistic ocean environments, including irregular and directional sea states. This would help assess the robustness of the propulsion mechanism, directional control and operational performance beyond the regular wave conditions considered in the present study.

CRediT authorship contribution statement

Milad Zabihi: Data curation, Formal analysis, Investigation, Methodology, Validation, Visualization, Writing – original draft, Writing – review & editing. **V.V.S. Sricharan:** Data curation, Formal analysis, Investigation, Methodology, Software, Validation, Visualization, Writing – original draft, Writing – review & editing. **Ayse Nur Karayel:** Formal analysis, Investigation, Visualization, Writing – review & editing. **Brendan McGrath:** Conceptualization, Investigation, Writing – review & editing. **Patrick Duffy:** Conceptualization, Investigation, Writing – review & editing. **Jimmy Murphy:** Methodology, Supervision, Writing – review & editing.

Declaration of competing interest

The authors declare the following financial interests/personal relationships which may be considered as potential competing interests: Patrick Duffy has patent #3334925 issued to Patrick Duffy. If there are other authors, they declare that they have no known competing financial interests or personal relationships that could have appeared to influence the work reported in this paper.

Acknowledgements

The authors are thankful for the support given by Sustainable Energy Authority of Ireland (SEAI) and Lir National Ocean Test Facility staff.

References

Bertram, V., 2008. Unmanned surface vehicles-a survey. Skibsteknisk Selskab, Copenhagen, Denmark 1, 1–14.
Boscaino, V., Odetti, A., Marsala, G., Di Cara, D., Panzavecchia, N., Caccia, M., Tine, G., 2021. A fuel cell powered autonomous surface vehicle: the Eco-SWAMP project. Int. J. Hydrogen Energy 46, 20732–20749.
Breivik, M., 2010. Morten Breivik Topics in Guided Motion Control of Marine Vehicles.
Breivik, M., Hovstein, V.E., Fossen, T.I., 2008. Straight-Line Target Tracking for Unmanned Surface Vehicles.
Caccia, M., Bono, R., Bruzzone, G., Spirandelli, E., Veruggio, G., Stortini, A.M., Capodaglio, G., 2005. Sampling sea surfaces with SESAMO: an autonomous craft for the study of sea-air interactions. IEEE Robot. Autom. Mag. 12, 95–105.
Chao, Y., 2016. Autonomous underwater vehicles and sensors powered by ocean thermal energy. In: OCEANS 2016-Shanghai. IEEE, pp. 1–4.
Crimmins, D.M., Patty, C.T., Beliard, M.A., Baker, J., Jalbert, J.C., Komerska, R.J., Chappell, S.G., Blidberg, D.R., 2006. Long-endurance test results of the solar-powered AUV system. In: OCEANS 2006. IEEE, pp. 1–5.
Ding, W., Song, B., Mao, Z., Wang, K., 2015. Experimental investigation on an ocean kinetic energy harvester for underwater gliders. 2015 IEEE Energy Conversion Congress and Exposition (ECCE). IEEE, pp. 1035–1038.
Donelan, M.A., Drennan, W.M., Katsaros, K.B., 1997. The air–sea momentum flux in conditions of wind sea and swell. J. Phys. Oceanogr. 27, 2087–2099.
Er, M.J., Ma, C., Liu, T., Gong, H., 2023. Intelligent motion control of unmanned surface vehicles: a critical review. Ocean. Eng. https://doi.org/10.1016/j.oceaneng.2023.114562.
Falcao, A.F. de O., 2010. Wave energy utilization: a review of the technologies. Renew. Sustain. Energy Rev. 14, 899–918.
Hine, R., Willcox, S., Hine, G., Richardson, T., 2009. The wave glider: a wave-powered autonomous marine vehicle. In: OCEANS 2009. IEEE, pp. 1–6.
ITTC, Recommended Procedures and Guidelines, Uncertainty Analysis for a Wave Energy Converter. ITTC report: 7.5-02-07-03.12.
Judge, F.M., Lyden, E., O'Shea, M., Flannery, B., Murphy, J., 2021. Uncertainty in wave basin testing of a fixed oscillating water column wave energy converter. ASCE-ASME J. Risk Uncertain. Eng. Syst. Part B Mech. Eng. 7. https://doi.org/10.1115/1.4051164.
Kiencke, U., Nielsen, L., Sutton, R., Schilling, K., Papageorgiou, M., Asama, H., 2006. The impact of automatic control on recent developments in transportation and vehicle systems. Annu. Rev. Control 30, 81–89.
Liu, Z., Zhang, Y., Yu, X., Yuan, C., 2016. Unmanned surface vehicles: an overview of developments and challenges. Annu. Rev. Control. https://doi.org/10.1016/j.arcontrol.2016.04.018.
López, I., Andreu, J., Ceballos, S., De Alegría, I.M., Kortabarria, I., 2013. Review of wave energy technologies and the necessary power-equipment. Renew. Sustain. Energy Rev. 27, 413–434.
Manley, J.E., 2008. Unmanned surface vehicles, 15 years of development. In: OCEANS 2008. Ieee, pp. 1–4.
Manley, J., Willcox, S., 2010. The wave glider: a new concept for deploying ocean instrumentation. IEEE Instrum. Meas. Mag. 13, 8–13.
Motwani, A., 2012. A survey of uninhabited surface vehicles. Marine and Industrial Dynamic Analysis, School of Marine Science and Engineering. Plymouth University, Tech. Rep.
Orcina, 2025. OrcaFlex (version 11.2c). www.orcina.com/orcaflex/.
Pastore, T., Djapic, V., 2010. Improving autonomy and control of autonomous surface vehicles in port protection and mine countermeasure scenarios. J. Field Robot. 27, 903–914.
Petersen, S., Krätschell, A., Augustin, N., Jamieson, J., Hein, J.R., Hannington, M.D., 2016. News from the seabed – geological characteristics and resource potential of deep-sea mineral resources. Mar. Pol. 70, 175–187. https://doi.org/10.1016/j.marpol.2016.03.012.
Rasal, K., 2013. Navigation & Control of an Automated Swath Surface Vessel for Bathymetric Mapping.
Rehman, S., Alhems, L.M., Alam, M.M., Wang, L., Toor, Z., 2023. A review of energy extraction from wind and ocean: technologies, merits, efficiencies, and cost. Ocean. Eng. 267, 113192.
Roberts, G.N., Sutton, R., 2006. Advances in Unmanned Marine Vehicles. Iet.
Samad, A., Suchithra, R., 2021. Marine power Technology—Wave energy. In: Sustainable Fuel Technologies Handbook. Elsevier, pp. 241–267.
Shore Protection Manual, 1984. Department of the Army, Waterways Experiment Station, Corps of Engineers, and. Coastal Engineering Research Center.
Sornek, K., Wiercioch, J., Kurczyna, D., Figaj, R., Wójcik, B., Borowicz, M., Wieliński, M., 2022. Development of a solar-powered small autonomous surface vehicle for environmental measurements. Energy Convers. Manag. 267, 115953.
Townsend, N., 2016. In Situ Results from a New Energy Scavenging System for an Autonomous Underwater Vehicle.
Townsend, N.C., Shenoi, R.A., 2016. Feasibility study of a new energy scavenging system for an autonomous underwater vehicle. Auton. Robots 40, 973–985.
Švec, P., Thakur, A., Raboin, E., Shah, B.C., Gupta, S.K., 2014. Target following with motion prediction for unmanned surface vehicle operating in cluttered environments. Auton. Robots 36, 383–405.
Veerabhadrappa, K., Suhas, B.G., Mangrulkar, C.K., Kumar, R.S., Mudakappanavar, V.S., Seetharamu, K.N., 2022. Power generation using ocean waves: a review. Global Transitions Proceedings 3, 359–370.
Wang, X., Shang, J., Luo, Z., Tang, L., Zhang, X., Li, J., 2012. Reviews of power systems and environmental energy conversion for unmanned underwater vehicles. Renew. Sustain. Energy Rev. 16, 1958–1970.
Willcox, S., Manley, J., Wiggins, S., 2009. The wave glider, an energy harvesting autonomous surface vessel. Sea Technol. 49, 29–31.
Yang, Y., Martinez, E., 2023. Feasibility analysis of a wave powered autonomous underwater vehicle. Energy Convers. Manag. X 18, 100352.
Zabihi, M., Mazaheri, S., Namin, M.M., 2019. Experimental hydrodynamic investigation of a fixed offshore oscillating water column device. Appl. Ocean Res. 85, 20–33. https://doi.org/10.1016/j.apor.2019.01.036.
Zhang, Y., Yang, F., Li, Y., Qiu, W., 2021. Design and numerical investigation of a multi-directional energy-harvesting device for UUVs. Inside Energy 214, 118978.